STRUCTURAL PROPERTIES AND PHASE BEHAVIOR IN COLLOIDAL SUSPENSIONS

BY

STEPHEN AUSTIN BARR

DISSERTATION

Submitted in partial fulfillment of the requirements
for the degree of Doctor of Philosophy in Materials Science and Engineering
in the Graduate College of the
University of Illinois at Urbana-Champaign, 2010

Urbana, Illinois

Doctoral Committee:

Professor Erik Luijten, Chair
Professor Paul M. Goldbart
Professor Jennifer Lewis
Professor Kenneth Schweizer

ABSTRACT

In this dissertation I present my research on the effective interactions of colloidal particles induced by a smaller species, as well as the structure of colloidal particles undergoing freeze casting. In this research I have used a wide variety of computational techniques in order to understand these systems.

Specifically, in Chapter 2 I study nanoparticle haloing in a system of silica microspheres and highly charged polystyrene nanoparticles. Computer simulations are employed to determine the effective microsphere–microsphere potential induced by the nanoparticles. From these simulations I am also able to determine the degree of nanoparticle adsorption on the microsphere surface.

In Chapter 3 I investigate the depletion interaction in a system of charged microspheres and rigid rods. The effect of both rod concentration and screening length is explored.

In Chapter 4 I study the effective interactions between charged colloids in the presence of multivalent counterions. The role of colloid charge is investigated and the onset of like-charged attraction is determined and compared with theoretical predictions. In order to study this system, I extended the geometric cluster algorithm to efficiently simulate systems interacting through the Coulomb potential.

In Chapter 5 computer simulations are employed to elucidate the experimentally observed crystal phases of the Qβ and MS-2 virus particles in solution with multivalent salt and non-adsorbing polymer.

Freeze casting is studied in Chapter 6. In this process colloidal particles are pushed by an advancing ice front. I use molecular dynamics simulations to study the dynamics of the colloidal particles and the resulting structures formed.

To my family.

ACKNOWLEDGMENTS

I would not have been able to complete this work without the support of many people. Thanks to my adviser, Erik Luijten, for guidance during my my Ph.D. study. Thanks to Wonki Roh, Daniel Sinkovits, Camilo Guáqueta, and Jon Whitmer for many helpful discussions and making my time at UIUC enjoyable. Finally, thanks to my wife, Christy, for her love and support.

TABLE OF CONTENTS

CHAPTER 1

INTRODUCTION

Colloidal suspensions display a rich phase behavior that can be controlled by tuning their interactions. This ability to tune the interactions allows colloids to be used in a variety of applications, including inks [1], paints [2], pharmaceuticals [3] and as precursors for advanced materials [4]. They are also used as model systems for atoms [5], since in addition to controlling the interactions, it is possible to directly observe the colloids, giving further insight into atomic phase transitions and dynamics. It is then the goal of this research to study the behavior of colloidal suspensions using computer simulations. We explore various methods to control colloidal interaction and also study their structure and dynamics in non-equilibrium systems.

One way in which colloidal interactions can be controlled is by introducing small additives to the suspension. Even at very low concentrations, these additives can have a large impact on colloidal interactions. In Chapter 2 we study this in a system of highly charged nanoparticles and weakly charged colloidal microspheres, focusing on the effect of nanoparticle concentration on the microsphere stability. Employing pair potentials that accurately represent silica–polystyrene mixtures that have been studied experimentally [6], we are able to demonstrate that nanoparticle-induced stabilization can arise from a relatively weak van der Waals attraction between the colloids and nanoparticles. This demonstrates that the nanoparticle haloing mechanism [7] for colloidal stabilization is of considerable generality and potentially can be applied to large classes of systems.

We continue to explore the effect of additives in Chapter 3. In this case, however, we consider non-spherical particles, specifically rods. These offer an interesting alternative to spherical particles since they have been shown to produce a stronger depletion attraction at the same volume fraction [8]. We study this in a system of rigid rods and colloidal microspheres where both have a negative charge, focusing on the effect of rod concentration and screening length.

In Chapter 4 we investigate the effect of colloid charge on the interactions between like-charged colloids in the presence of multivalent counterions by means of computer simulations. Owing to the size asymmetry

between the ions and the colloids, we use the generalized geometric cluster algorithm (GCA) [9, 10]. Because ions are included explicitly, we use the Coulomb potential between all charged particles, and while any pair potential can be used with the GCA in general, the long-range nature of the Coulomb potential causes the simulations to become very inefficient. To overcome this we modify the GCA to efficiently simulate charged systems. We find that in the presence of multivalent counterions, like-charged attraction between the colloids occurs above a critical colloid charge which increases with increasing colloid size. We also find that at fixed colloid size, the strength of the attraction increases linearly with increasing colloid charge.

In Chapter 5 we investigate the crystal phases formed by the Qβ and MS-2 viruses in the presence of multivalent salt and non-adsorbing polymer. Both virus particles are spherical and have a net negative charge due to the RNA in their cores. The charged states of the amino acids in their protein coat, however, lead to an inhomogeneous surface charge distribution which differs for Qβ and MS-2. This leads to different observed crystal phases for the two viruses, and, in the case of Qβ, a transition in crystal structure with increasing polymer concentration. We explore this system by using grand-canonical Monte Carlo simulations to explicitly include salt, and measuring the osmotic pressure as a function of lattice spacing for different crystal structures. We find that at low polymer concentrations, the system must overcome a free energy barrier to form a stable crystal and that the barrier height is different for different crystal structures, leading one phase to be favored kinetically in this regime. The addition of more polymer eliminates this barrier.

Finally, in Chapter 6 we study the structure and dynamics of colloidal particles undergoing freeze casting. In this process, an aqueous suspension of colloidal particles is frozen under specific conditions which result in the formation of ice platelets or dendrites with high aspect ratios that engulf or reject the particles, depending on their size and the velocity of the advancing ice front [11]. As the particles are pushed between the growing crystals, concentrated regions of colloidal particles are formed. Recent experiments have exploited this to create strong, porous materials with a well-controlled microstructure [12, 13]. We investigate this process by means of molecular dynamics simulations, focusing on the effect of the ice front velocity on the structure of the resulting material. We develop a model that accounts for particle engulfment or rejection by the ice front, and study both columnar and lamellar geometries. The degree of order of the resulting solid and the thickness of the walls surrounding the pores are shown to be determined by front velocity and initial particle concentration in the suspension.

CHAPTER 2

NANOPARTICLE HALOING

The contents of this chapter are based on the following publication:

- **Stephen A. Barr** and Erik Luijten, Effective Interactions in Mixtures of Silica Microspheres and Polystyrene Nanoparticles, *Langmuir*, 22:7152–7155, 2006

In most colloidal systems of interest, there is an attraction between the particles due to van der Waals forces, resulting in flocculation. In order to prevent this, the van der Waals forces must be balanced, which can be accomplished by charge [14] or steric stabilization [15]. In addition, a new method, referred to as "nanoparticle haloing" was reported [7, 16]. In these experiments, a small volume fraction of highly charged zirconia nanoparticles was found to stabilize silica microspheres against flocculation, even though the nanoparticles did not strongly adsorb on the microsphere surface. Liu and Luijten have shown that stabilization can result from a *weak* colloid–nanoparticle attraction which causes a shell of nanoparticles to form around the microspheres, resulting in an effective repulsion [17, 18]. Analytical calculations based on an integral-equation approach have shown that electrostatic repulsion between the nanoparticles in the absence of an any colloid–nanoparticle attraction can also result in the nanoparticles segregating to the microsphere surface, albeit at a much larger Debye screening length than seen in the experiments [19]. It was also observed that sufficiently high nanoparticle concentrations result in reentrant gelation, which is ascribed to a depletion attraction between the colloids [7]. Computer simulations [17] and analytical approaches [19] have recovered this attraction as well.

The potential impact of this new colloidal stabilization technique makes it highly desirable to demonstrate its general applicability and to obtain a more complete understanding. The complex solution chemistry in the original experiments [7, 16] made it difficult to accurately characterize the colloidal interactions.

Since these interactions provide the starting point for particle-based simulations, it is thus of great interest that recently Chan and Lewis have performed experiments on binary mixtures that have a similar size and charge asymmetry, but for which the interactions are better characterized [6]. In these experiments, the zirconia nanoparticles are replaced by polystyrene particles, and three different systems are investigated. Two cases exhibit unsurprising behavior, namely negatively charged colloids (silica at $p\mathrm{H} = 5$) with either amidine polystyrene (cationic) or sulfate polystyrene (anionic) nanoparticles. In these systems, there is either a strong attraction or a strong repulsion between colloids and nanoparticles, resulting in strong adsorption or virtually no adsorption. Without adsorption, the silica microspheres are stabilized by their direct electrostatic repulsion, whereas the strongly adsorbing case leads to "bridging" flocculation. The third and most interesting case corresponds to weakly charged colloids ($p\mathrm{H} = 3$, zeta potential $\zeta_{\mathrm{micro}} = -1$ mV) with sulfate polystyrene nanoparticles ($\zeta_{\mathrm{nano}} = -120$ mV). Under these conditions, the electrostatic interaction between the microspheres is overwhelmed by their van der Waals attraction. Nevertheless, stabilization is observed in the presence of nanoparticles. This is particularly remarkable because the electrostatic colloid–nanoparticle interaction is expected to be negligibly small and measurements indeed indicate only weak adsorption of the nanoparticles to the microsphere surface. In this chapter we investigate this system by means of large-scale computer simulations in order to explain the experimental observations and clarify their relation to the original nanoparticle haloing observations.

2.1 Simulation details

In order to study nanoparticle haloing we adopt the following model system based on the experiments of Chan and Lewis [6]. Both the colloidal microspheres and the nanoparticles are modeled as hard spheres, with respective diameters of $\sigma_{\mathrm{micro}} = 1.18\ \mu$m and $\sigma_{\mathrm{nano}} = 19$ nm. In addition to the hard-sphere potential, the nanoparticles have an electrostatic repulsion V_{nano} and the microsphere–nanoparticle interaction $V_{\mathrm{m-n}}$ consists of a van der Waals attraction and a (weak) electrostatic repulsion. All potentials are calculated as outlined in the supporting information of Ref. [6]. The solvent and salt are modeled implicitly as a dielectric continuum, leading to screened electrostatic interactions that are obtained via the linear superposition approximation [20], with a Debye screening length of 9.6 nm. The van der Waals interaction is calculated using Lifshitz theory [21], resulting in a microsphere–nanoparticle interaction that has an attractive well at contact followed by a weak repulsive barrier comparable to the thermal energy, $k_{\mathrm{B}}T$, where k_{B} is Boltz-

mann's constant and $T = 298$ K indicates the absolute temperature. All calculations are performed in the canonical (constant-NVT) ensemble, using MC simulations. A cubic simulation box with periodic boundary conditions is used. Due to the large size ratio between the microspheres and the nanoparticles, we use the geometric cluster algorithm (GCA) which has been shown to be much more efficient than conventional simulation methods under these conditions [9, 10].

It is important to note that the microsphere–nanoparticle attraction strength diverges at contact. This leads to an unphysically strong degree of nanoparticle adsorption, which in real systems is prevented by surface roughness. To take this into account we truncate the potential well at a surface separation $D_{\rm cut}$, given by the condition $V_{\rm m-n}(D_{\rm cut}) = V_{\rm cut}$. For smaller separations $0 < D < D_{\rm cut}$, we set the potential to a constant value $V_{\rm cut}$. The resulting potential is depicted in Fig. 2.1, for $V_{\rm cut} = -7.5\ k_{\rm B}T$. We use the observed degree of nanoparticle adsorption as a measure to calibrate $V_{\rm cut}$ and investigate three different choices for this cutoff, namely $V_{\rm cut}/(k_{\rm B}T) = -10$, -7.5, and -5.0.

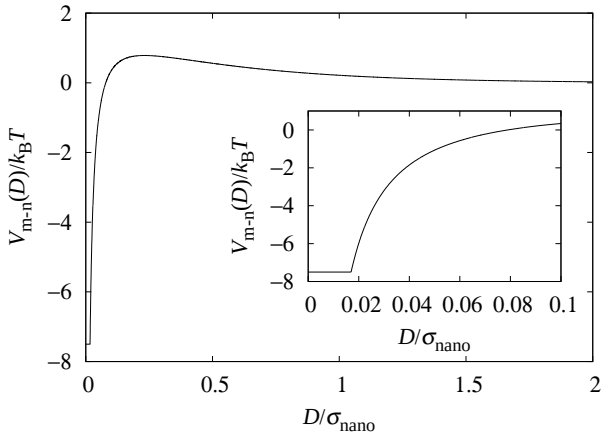

Figure 2.1: The colloid–nanoparticle potential resulting from a van der Waals attraction and a weak electrostatic repulsion. In this example, the minimum in the potential is cutoff at $-7.5\ k_{\rm B}T$. The inset shows a magnified view near contact. All values that would be lower than $V_{\rm cut}$ are set to $V_{\rm cut}$ which causes a small flat region near contact. Beyond $D/\sigma_{\rm nano} = 13.5$ the potential is set to zero.

2.2 Surface coverage

We first investigate the degree of nanoparticle adsorption on the microsphere surface. In these calculations we use 10 microspheres at a volume fraction $\phi_{\rm micro} = 0.10$. For each value of $V_{\rm cut}$ we find that the colloid–nanoparticle pair correlation function has a maximum at contact followed by a minimum at a separation of approximately 5 nm. We determine the degree of adsorbed nanoparticles by counting the average number

of particles with a smaller surface separation than this minimum. Figure 2.2 displays the resulting number of adsorbed nanoparticles per microsphere, $N_{\text{nano}}^{\text{ads}}$, as a function of nanoparticle volume fraction ϕ_{nano}, along with the experimental data [6]. The degree of adsorption increases with increasing magnitude of V_{cut} and at low nanoparticle concentration approaches 100% for $V_{\text{cut}} = -10\ k_{\text{B}}T$. Upon increase of the nanoparticle concentration, the number of adsorbed particles initially increases approximately linearly with ϕ_{nano}, but levels off at higher concentrations. A similar plateau was observed in earlier simulations [17] and is due to the electrostatic repulsion between adsorbed nanoparticles. The experimental results were obtained by measuring the fluorescence intensity of the supernatant solution in systems with labeled polystyrene particles and behaves somewhat irregularly. At low concentrations, virtually 100% adsorption is found, followed by a *decrease* in adsorption. At high ϕ_{nano} the uncertainties become very large. Although it is not possible to accurately determine V_{cut} from this comparison, it appears reasonable to conclude that the optimal value describing the experimental data is bracketed by our choices for V_{cut}.

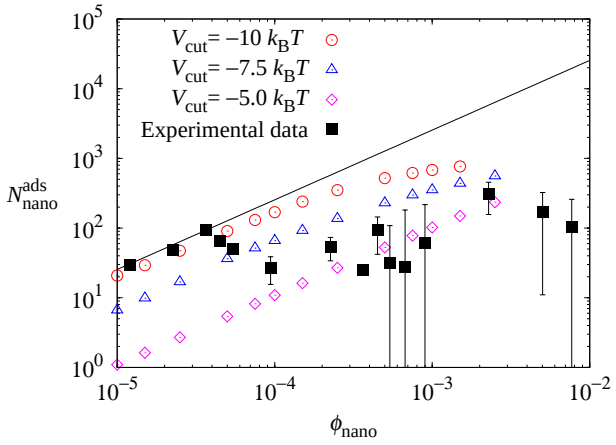

Figure 2.2: Surface coverage (in units of adsorbed nanoparticles per microsphere) as a function of nanoparticle concentration. The filled symbols represent the experimental data [6] and the solid line represents 100% nanoparticle adsorption. The uncertainty in the numerical data is negligibly small on the scale of this plot. As the magnitude of the potential-well cutoff is increased (*cf.* Fig. 2.1), the degree of adsorption increases accordingly.

2.3 Effective interactions

In order to determine the range of nanoparticle concentrations that stabilizes the microspheres, we determine the effective microsphere–microsphere potential, $V_{\text{micro}}^{\text{eff}}$. This potential is induced by the nanoparticles and is independent of the direct microsphere–microsphere potential [18, 22]. Because of this, we can omit the

electrostatic and van der Waals interactions between the microspheres in the simulations. The effective interaction is then determined from the microsphere pair correlation function $g(r)$ via $V^{\rm eff}(r) = -k_{\rm B}T \ln[g(r)]$, provided that many-body effects are eliminated. This is accomplished by working in the dilute limit, $\phi_{\rm micro} = 0.01$. At fixed $\phi_{\rm nano}$, the computational effort is linearly proportional to the number of microspheres, whereas the number of sampled pair separations increases quadratically. Even though many of these additional samples are at large separations, it is still advantageous to use a larger number of microspheres. We therefore use 10 microspheres (rather than the minimum number of 2) in all calculations. The nanoparticle volume fraction is varied from $\phi_{\rm nano} = 10^{-5}$ to $\phi_{\rm nano} = 6.5 \times 10^{-3}$, which corresponds to a maximum of more than 1.5×10^6 nanoparticles. The GCA proves indispensable for these calculations, since it is essential to equilibrate both the microspheres and the surrounding distribution of nanoparticles. The pairwise interactions are sufficiently strong to result in quite large energy variations if arbitrary particle displacements are imposed, leading to very small acceptance rates (or very small displacements) in a conventional MC simulation. On the other hand, the pairwise interactions are sufficiently weak to maintain a relatively homogeneous distribution of nanoparticles. Consequently, there is a significant probability of hard-sphere overlaps if a microsphere is displaced, which would again result in a rejected move in a conventional MC approach. The GCA resolves both issues, permitting an efficient exploration of phase space. For each choice of $V_{\rm cut}$ and $\phi_{\rm nano}$ we construct between 3.0×10^6 and 51×10^6 clusters, which corresponds to $(0.33\text{–}5.7)\times 10^6$ Monte Carlo sweeps (where a sweep is defined by an update of all large particle positions). There are between 100 and 4000 nanoparticles in each cluster. Because the GCA guarantees that these are updated at a rate that is controlled by their degree of interaction with the microspheres, their relaxation is very efficient.

The effective pair interaction, $V^{\rm eff}_{\rm micro}$ is shown as a function of the microsphere separation for different values of $\phi_{\rm nano}$ with $V_{\rm cut} = -10\ k_{\rm B}T$ in Fig 2.3. There is a strong attractive minimum at short separations arising from a bridging attraction in which a single nanoparticle is adsorbed to two microspheres. Closer to contact, the total microsphere interaction (not shown) has an additional minimum owing to the van der Waals attraction between the microsphere. However, if two microspheres approach, then these minima are preceded by a repulsive barrier which rapidly increases in height with increasing $\phi_{\rm nano}$. Note that at the position of this barrier the van der Waals attraction is already negligibly small, so $V^{\rm eff}_{\rm micro}$ in Fig. 2.3 represents the total microsphere interaction. We estimate that kinetic stabilization occurs for a potential barrier around

4 k_BT to 5 k_BT, corresponding to a threshold concentration, ϕ_{nano}^{stable}, of approximately 10^{-4}. (Because the barrier height increases rapidly with increasing ϕ_{nano}, our result for ϕ_{nano}^{stable} does not depend sensitively on the precise criterion for the required barrier height.) This is considerably lower than the experimental result [6] of $\phi_{nano}^{stable} \approx 6 \times 10^{-4}$, which is not surprising, as the choice of $V_{cut} = -10\ k_BT$ overestimates the degree of nanoparticle adsorption (*cf.* Fig. 2.2). Accordingly, we repeat the calculations for $V_{cut} = -7.5\ k_BT$, shown in Fig. 2.4. We see the same qualitative behavior, but almost 7 times higher nanoparticle concentrations are required to attain repulsive barriers of the magnitude shown in Fig. 2.3. Specifically, we estimate $\phi_{nano}^{stable} \approx 7 \times 10^{-4}$, in good agreement with the experimental value. As shown in Fig. 2.2, at this threshold concentration only several hundred nanoparticles are adsorbed on each microsphere. Interestingly, if we raise V_{cut} to $-5.0\ k_BT$, we never observe a barrier that is high enough to achieve stabilization; even at $\phi_{nano} = 3.5 \times 10^{-3}$ it reaches a maximum of only 2 k_BT, shown in Fig. 2.5.

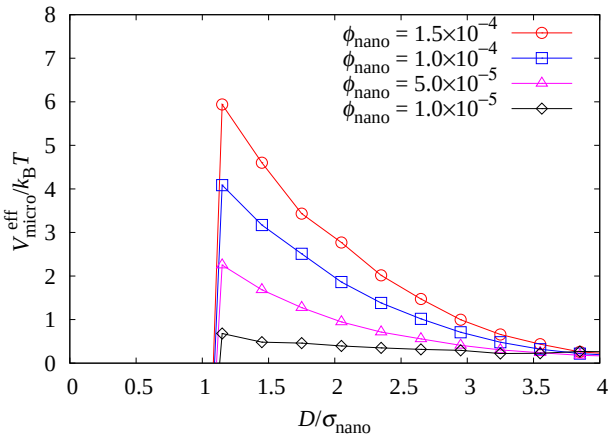

Figure 2.3: The effective colloid–colloid interaction for different values of ϕ_{nano}, for $V_{cut} = -10\ k_BT$. The nanoparticles induce an effective barrier with a height that increases with increasing ϕ_{nano} and reaches a value large enough to induce stabilization at $\phi_{nano} = 10^{-4}$, significantly lower than the value that is found experimentally of $\phi_{nano} = 6 \times 10^{-4}$. The sharp decrease at σ_{nano} is caused by a bridging configuration when one nanoparticle adsorbs to two microspheres.

For a system with an electrostatically induced colloid–nanoparticle attraction, it was found in Ref. [17] that upon further increase in nanoparticle concentration the effective microsphere potential develops an attractive minimum at a particle separation that exceeds the position of the barrier. To investigate whether this phenomenon also occurs when the weak nanoparticle adsorption is driven by a van der Waals attraction, we perform simulations at values of ϕ_{nano} larger than 10^{-3}. Owing to the sheer number of particles, these calculations are computationally very demanding. In addition, the strong repulsion between nanoparticles makes their *effective* volume fraction relatively high, which affects the efficiency of the GCA [9]. Never-

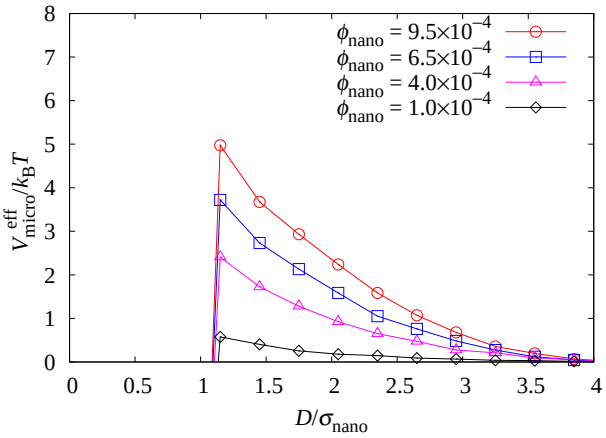

Figure 2.4: $V^{\text{eff}}_{\text{micro}}$ is shown at different values of ϕ_{nano} for $V_{\text{cut}} = -7.5\ k_{\text{B}}T$. The barrier height increases with increasing ϕ_{nano} and reaches a value large enough to induce stabilization at $\phi_{\text{nano}} = 6.5 \times 10^{-4}$, close to the value that is found experimentally of $\phi_{\text{nano}} = 6 \times 10^{-4}$.

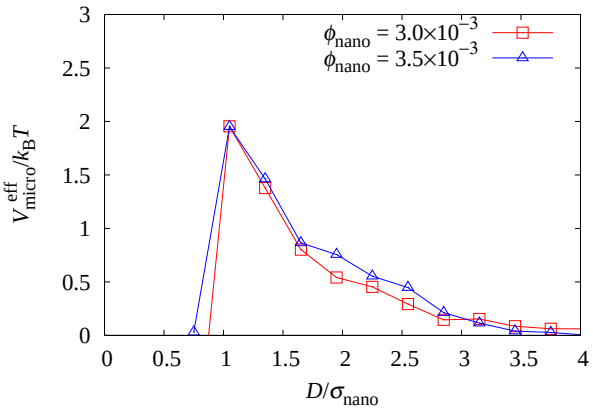

Figure 2.5: $V^{\text{eff}}_{\text{micro}}$ is shown at different values of ϕ_{nano} for $V_{\text{cut}} = -5\ k_{\text{B}}T$. The barrier is not high enough to stabilize the colloids. Even at $\phi_{\text{nano}} = 3.5 \times 10^{-3}$, the maximum is only $2\ k_{\text{B}}T$.

theless, Fig. 2.6 indeed shows the development of a secondary minimum in $V^{\text{eff}}_{\text{micro}}$ as ϕ_{nano} is increased. In accordance with earlier findings [10, 17] the minimum occurs at a microsphere surface separation between 3 and 4 nanoparticle diameters and rapidly becomes deeper at larger ϕ_{nano}. At $\phi_{\text{nano}} = 6.0 \times 10^{-3}$, the attraction is close to $-1\ k_{\text{B}}T$ and we estimate it to exceed $-3\ k_{\text{B}}T$ for concentrations somewhat above 10^{-2}. This attraction will be sufficient to give rise to reentrant gelation, in good agreement with the experimental observations [6].

It has been proposed that asymmetric binary mixtures can be understood via an (approximate) mapping onto nonadditive hard-sphere mixtures, which in turn can be analyzed by an exact mapping onto an additive hard-sphere model [23]. Applied to the system studied here, both the repulsion between nanoparticles and

the nanoparticle–microsphere attraction lead to a negative nonadditivity. Interestingly, it was found that such negative nonadditivity indeed leads to generalized depletion potentials with features similar to those that we find in the effective potential $V_{\mathrm{micro}}^{\mathrm{eff}}$, namely, a repulsive barrier near contact followed by a second attractive minimum [23, 24] both of which are enhanced compared to an additive hard-sphere mixture [25].

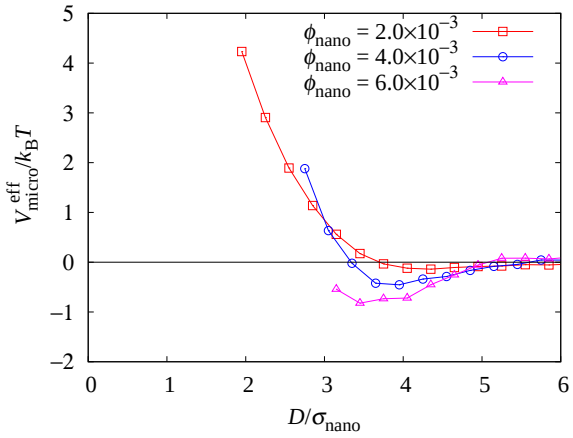

Figure 2.6: $V_{\mathrm{micro}}^{\mathrm{eff}}$ for $\phi_{\mathrm{nano}} > 10^{-3}$ using $V_{\mathrm{cut}} = -7.5\ k_{\mathrm{B}}T$. At the higher concentrations shown here the repulsive barrier persists. More important, however, is that an attractive minimum develops for microsphere separations of $3\sigma_{\mathrm{nano}} < D < 4\sigma_{\mathrm{nano}}$. This minimum is estimated to reach a value of around $-3\ k_{\mathrm{B}}T$ for $\phi_{\mathrm{nano}} \approx 10^{-2}$, resulting in gelation.

2.4 Summary and conclusions

In summary, we have studied the effective interactions in binary mixtures of silica microspheres and small concentrations of highly charged polystyrene nanoparticles. We have used a model that is sufficiently coarse-grained to permit equilibrium calculations for large-scale systems (up to 1.5×10^6 particles) but that also employs potentials that accurately describe the pairwise interactions, permitting direct comparison with relevant experimental work [6]. In particular, we incorporate the van der Waals attraction between nanoparticles and microspheres, which is responsible for weak adsorption of the nanoparticles. Our findings lead to the following conclusions. (i) Highly charged nanoparticles can kinetically stabilize colloidal microspheres even if the colloid–nanoparticle attraction results from a van der Waals attraction rather than from an induced electrostatic attraction [17]. This confirms experimental observations [6] and corroborates that nanoparticle haloing relies on generic features and hence should be of considerable generality. (ii) The required volume fraction of nanoparticles at the onset of stability can be controlled by tuning the

strength of the nanoparticle–microsphere attraction. (iii) Although experimentally the observed number of adsorbed nanoparticles is considered to be negligible [6], our calculations show that already several hundred nanoparticles per microsphere give rise to an effective microsphere repulsion that is sufficient for kinetic stabilization.

CHAPTER 3

DEPLETION INDUCED BY CHARGED RODS

Depletion interactions are common in colloidal systems, occurring whenever larger particles are in suspension with either smaller colloidal particles or non-adsorbing polymer. Since they cannot overlap, small particles are excluded from a region around the larger particles, called the depletion region. If the depletion regions of two large particles overlap, the small particles gain free volume, and therefore translational entropy. This leads to an effective attraction between the larger particles, where the range is controlled by the small particle diameter and the strength is controlled by the small particle concentration [26]. While the use of hard spheres [24, 25, 27] and polymers [28, 29] as depletion agents is well understood, less in known about the effect of non-spherical depletants. Recently, however, experiments have been performed investigating the depletion interaction caused by charged rigid rods [30, 31].

In addition to these experiments, rigid rod depletants have been the subject of theoretical investigations [8, 32–36] and simulations [37]. However, these have only considered systems with hard interactions, modeling the rods as either infinitely thin needles or hard spherocylinders. Additional soft interactions, for example resulting from charge, are difficult to treat theoretically, but may have a large impact on the resulting properties of the suspension. In this chapter we use MC simulations to investigate the role of these interactions. The effects of both the screening length and the rod concentration are investigated. We also study the effects of particle anisotropy by comparing systems with rods to similar systems with spherical depletants.

3.1 Simulation method

We adopt the following model system to study the depletion attraction induced by charged rigid rods, based on the experiments of Helden *et al.* [31] which consider a suspension of polystyrene microspheres and silica coated boehmite (γ-AlOOH) rods. The polystyrene microspheres are modeled as hard spheres with

diameter $\sigma_{\text{micro}} = 3.7\ \mu$m. The rods are constructed out of 11 interaction sites, placed 18 nm apart in a line, each with a hard sphere diameter $\sigma_{\text{rod}} = 18$ nm for a total rod length of 198 nm. The salt and solvent are modeled implicitly, leading to charged interactions modeled by a screened electrostatic potential [38] given by

$$\frac{V(r)}{k_{\text{B}}T} = Z_i Z_j \left(\frac{e^{\kappa a_i}}{1+\kappa a_i}\right)\left(\frac{e^{\kappa a_j}}{1+\kappa a_j}\right)\ell_{\text{B}} e^{-\kappa r}/r \tag{3.1}$$

where $\ell_{\text{B}} = e^2/(4\pi\varepsilon_0\varepsilon_r k_{\text{B}}T)$ is the Bjerrum length, Z_i is the charge of particle i with radius a_i, and κ is the inverse Debye screening length. The Bjerrum length is set to 0.714 nm corresponding to water at room temperature. The values for the charge are taken from the surface charge densities of polystyrene microspheres and silica coated rods which were determined by analyzing total internal reflection microscopy measurements of polystyrene and silica microspheres interacting with a silica surface [39]. The microsphere charge is 27000 and each interaction site of the rod has a charge of 4.2.

All calculations are performed in the canonical ensemble, using MC simulations and a cubic simulation box with periodic boundary conditions. Due to the size ratio between the rods and the spheres, we use the GCA [9, 10] as in Chapter 2. One issue with this it that the GCA updates particle positions using point reflections and this transformation does not relax the rotational degrees of freedom of the particles. To overcome this, in addition to cluster moves we perform rotational moves of individual rods using the standard Metropolis acceptance criterion [40–42]. For a given Monte Carlo step, we choose randomly between a cluster move and a rod rotation, however their probabilities are not equal. To ensure that the translational and rotational degrees of freedom of the rods decorrelate synchronously, we choose the probabilities such that there are, on average, as many rotational moves as there are rods in an average cluster move. This is determined from a short test run and we find there are between 300 and 3000 rods in an average cluster move. Because the rod concentrations studied are low, the acceptance rate for rotational moves is high, nearly 90% for a 180° rotation about an arbitrary axis, and this remains an efficient simulation method.

3.2 Effect of rod number

We first demonstrate how the effective microsphere–microsphere potential, $V_{\text{micro}}^{\text{eff}}$, changes as the rod concentration, ρ_{rod}, is increased. In all simulations, we use 4 microspheres at a volume fraction of $\phi_{\text{micro}} = 0.01$ to ensure we are in the dilute limit. As in Chapter 2, the effective interaction is determined from the mi-

crosphere pair correlation function $g(r)$ via $V^{\text{eff}}(r) = -k_{\text{B}}T \ln[g(r)]$. The screening length is fixed at $\kappa^{-1} = 21$ nm and the rod concentration is varied from from 24 μm^{-3} to 94 μm^{-3} which corresponds to 10^6 rods. In our simulations we never observe nematic ordering, which is not surprising given that the isotropic–nematic transition density for hard rods with the present aspect ratio is nearly 4000 μm^{-3} [43].

Figure 3.1 shows the resulting $V^{\text{eff}}_{\text{micro}}$. The depth of the depletion attraction increases with rod concentration and reaches a value close to $-1.5\ k_{\text{B}}T$ for $\rho_{\text{rod}} = 94\ \mu\text{m}^{-3}$. This is the usual trend for depletion attractions, however, we also observe that the location of the minimum moves to smaller separations as ρ_{rod} is increased and the potential well becomes narrower. This behavior is also observed in the experiments [31] and results from the competition between the direct electrostatic repulsion of the microspheres and the depletion attraction. A stronger attraction is able to overcome more of the direct repulsion, moving the minimum to smaller separations, and at these separations, both the depletion attraction and the direct repulsion are steeper, leading to the narrower well.

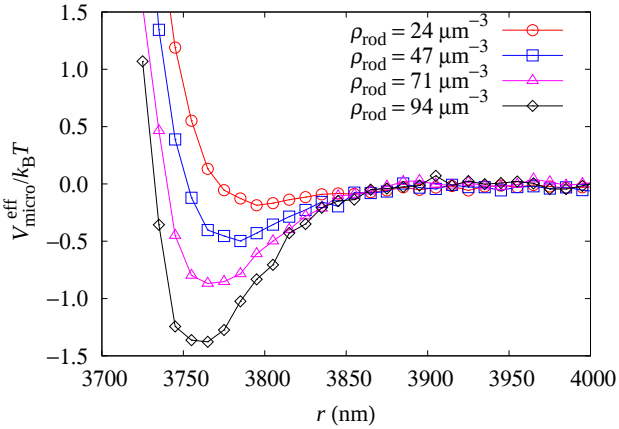

Figure 3.1: $V^{\text{eff}}_{\text{micro}}$ for different values of the rod concentration, ρ_{rod}. As the rod concentration is increased, the depletion potential becomes narrower and the minimum becomes deeper and moves closer to contact as a result of the competition between the direct repulsion and the depletion attraction, which is in qualitative agreement with the experimental results [31].

3.3 Effect of screening length

We also examine how $V^{\text{eff}}_{\text{micro}}$ is affected by the screening length, κ. Increasing the screening length has two effects on the depletion potential. The depletion region around the microspheres increases, owing to the increased repulsion between the rods and the microsphere, and this acts to enhance both the depth and

width of the minimum. At the same time, the rod–rod repulsion is enhanced in strength and range, leading to a larger effective size for the rods, and this acts to decrease the depletion attraction strength [23, 44]. In addition, the direct microsphere–microsphere repulsion is also enhanced in strength and range. Given these competing effects it is difficult to predict *a priori* how a change in κ will influence $V_{\text{micro}}^{\text{eff}}$.

For a rod density of 24 μm^{-3} we show $V_{\text{micro}}^{\text{eff}}$ in Fig. 3.2 as κ^{-1} is increased from 8.00 nm to 47.5 nm. The minimum moves to larger separations with increasing κ^{-1} as expected, however the strongest attraction is seen at the shortest screening length. To determine if this is due to the weaker repulsion between the microspheres at shorter screening lengths or a weaker depletion attraction at longer screening lengths we consider these contribution independently. By subtracting the direct microsphere–microsphere repulsion from $V_{\text{micro}}^{\text{eff}}$, we are left with only the depletion attraction induced by the rods, $V_{\text{micro}}^{\text{dep}}$, shown in Fig 3.3. From this we see that the depletion attraction increases dramatically with increasing κ^{-1}. It is clear that in this case, the trend seen in Fig. 3.2 results from the direct microsphere–microsphere repulsion becoming weaker compared with the depletion attraction at shorter screening lengths and not from the depletion attraction becoming stronger.

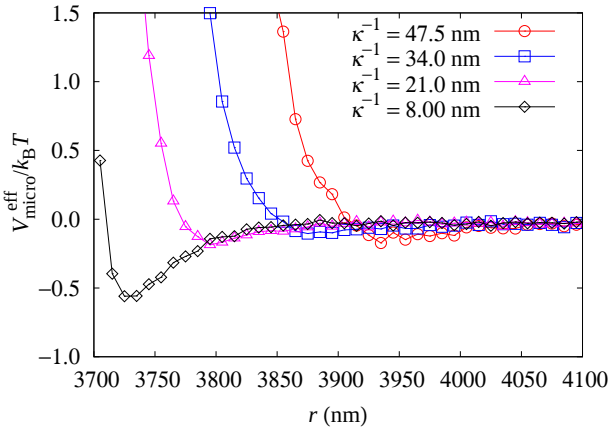

Figure 3.2: $V_{\text{micro}}^{\text{eff}}$ for a rod density of 24 μm^{-3} with different values of the screening length, κ^{-1}. As κ^{-1} is increased, the minimum moves to larger separations and becomes weaker.

When the rod density is increased to 71 μm^{-3} we observe a different trend. As for $\rho_{\text{rod}} = 24$ μm^{-3}, $V_{\text{micro}}^{\text{eff}}$ initially decreases in strength as κ^{-1} is increased. However, when $\kappa^{-1} = 47.5$ nm there is a large increase in the attraction strength with a depth of around 0.5 $k_{\text{B}}T$, as shown in Fig. 3.4. $V_{\text{micro}}^{\text{dep}}$ has the same trend as the lower rod concentration, however, in this case the depletion attraction starts to dominate at large κ^{-1}. This trend is also seen in the experiments and is attributed to the enhanced repulsion be-

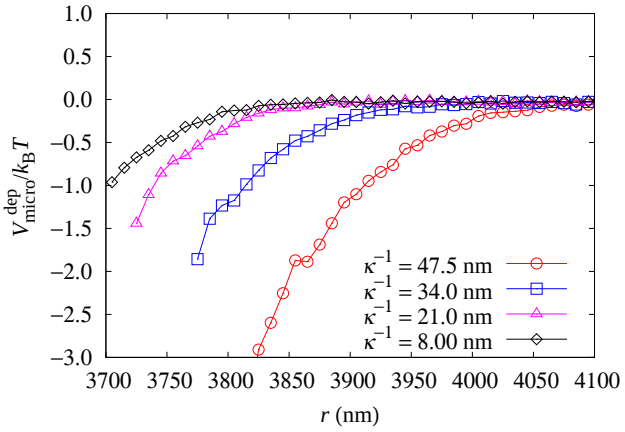

Figure 3.3: $V_{\text{micro}}^{\text{dep}}$ for a rod density of 24 μm^{-3} with different values of the screening length, κ^{-1}. As κ^{-1} is increased, the attraction induced by the rods becomes much stronger and longer ranged. For $\kappa^{-1} > 8.00$ nm we do not have any data for separations closer to contact because the direct microsphere–microsphere repulsion causes configurations with those separations to be very unfavorable.

tween the spheres and the rods [31]. These different trends occur because the depletion attraction and the direct microsphere–microsphere repulsion decay over different length scales. While the direct microsphere–microsphere repulsion is controlled only by κ, the range of the depletion attraction is controlled by κ and the rod length, which in this case is longer than the screening length. At this higher rod concentration the depletion attraction is stronger at larger separations where the direct microsphere repulsion has decayed.

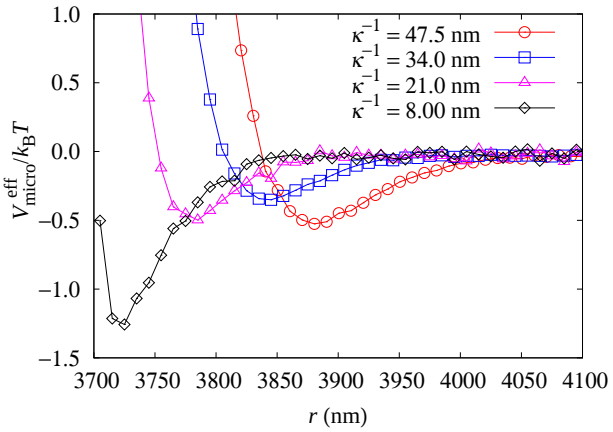

Figure 3.4: $V_{\text{micro}}^{\text{eff}}$ for a rod density of 71 μm^{-3} with different values of the screening length, κ^{-1}. As κ^{-1} is increased, the minimum moves to larger separations. The minimum initially decreases in strength with increasing κ^{-1}, however becomes stronger at $\kappa^{-1} = 47.5$ nm.

3.4 Comparison with spherical depletants

We now compare these results to the depletion attraction induced by spherical particles, which we test in two limits. In one limit, the sphere diameter, $\sigma_s = 18$ nm, is the same as the rod diameter and each sphere has a charge of 4.2. We set the volume fraction, ϕ_s, to 3.45×10^{-3}, matching the rod volume fraction for $\rho_{\text{rod}} = 71\ \mu\text{m}^{-3}$. This is analogous to breaking the rod into small spherical units. We also consider a system where $\sigma_s = 198$ nm, equal to the rod length. Here we keep the surface charge density of these spheres the same as the rods, resulting in a charge of 2152, and as before $\phi_s = 3.45 \times 10^{-3}$. In both cases, $\kappa^{-1} = 21$ nm.

As shown in Fig. 3.5, using rods results in a much stronger depletion attraction than spherical particles at the same volume fraction. When $\sigma_s = 18$ nm, the attraction range is small and is not able to overcome the the direct microsphere–microsphere repulsion over that range and therefore, no attraction is seen. When $\sigma_s = 198$ nm, the depletion interaction range is longer and there is a visible attraction, but the concentration is low and the resulting minimum is only about 0.2 $k_{\text{B}}T$ deep. Different choices can be made for the sphere diameter, where 18 nm $< \sigma_s <$ 198 nm, however we expect the resulting $V^{\text{eff}}_{\text{micro}}$ to lie between those two limits.

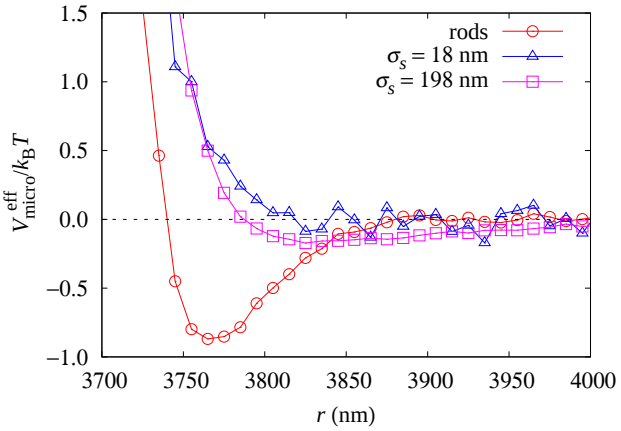

Figure 3.5: $V^{\text{eff}}_{\text{micro}}$ for spherical particles with diameter σ_s of 18 nm (triangles) and 198 nm (squares) compared with rods at a density of $\rho_{\text{rod}} = 71\ \mu\text{m}^{-3}$ (circles) with $\kappa^{-1} = 21$ nm (*cf.* Fig. 3.1). The depletion attraction of the small spheres is short-ranged and cannot overcome the direct microsphere–microsphere repulsion, whereas the larger spheres do not induce a strong attraction compared with rods at the same volume fraction.

3.5 Summary and conclusions

In conclusion, we have studied the effective interactions induced by charged rigid rods using large-scale computer simulations. The effect of rod concentration and screening length have been explored and in addition we have compared these results to spherical depletants. Increasing the rod concentration alters the effective microsphere–microsphere potential in three ways. It increases the well depth, results in a more narrow well, and moves the minimum to smaller separations. These observations are all a result of the competition between the depletion attraction and the direct microsphere–microsphere repulsion. Increasing the screening length results in a weaker depletion attraction for low rod concentrations, whereas for larger concentrations we see that the attraction strength at first decreases, then becomes stronger again for larger screening lengths. This results from the interplay between the range and strength of the depletion attraction and the direct microsphere–microsphere repulsion with increasing screening length. Finally, we found that rods induce a stronger depletion attraction than spherical particles at the same volume fraction, owing to their anisotropy. By understanding these effects, we gain insight into additional ways to control colloidal interactions.

CHAPTER 4

EFFECTIVE INTERACTIONS BETWEEN LIKE-CHARGED COLLOIDS

In this chapter we investigate the effect of multivalent ions on the interactions of charged spherical particles. Specifically, we are interested in understanding the attraction between like-charged colloidal particles in the presence of multivalent counterions. This phenomenon is not predicted by mean-field theories, such as DLVO theory [14,45], which instead predict purely repulsive electrostatic interactions between like-charged colloids under all conditions. One interesting note is that there have not been any experiments that observe like-charged attraction in bulk solution in the presence of multivalent counterions.

There have been a number of simulation studies of like-charged attraction, though, which have observed a short-ranged attraction between like-charged colloids in solution with multivalent counterions [46–51]. These simulations employed the primitive model where the ions and colloids are treated as charged hard spheres and the solvent enters only through its dielectric constant. In aqueous solution, these simulations have been limited to small colloids with diameters in the range of 2-4 nm [46–50], though like-charged attraction has been seen in simulations of larger colloids with a diameter of about 100 nm in a solvent with a dielectric constant of 2 [51].

This phenomenon has also been studied using theoretical methods. Work done by Rouzina and Bloomfield [52] focusing on plates concluded that like-charged attraction occurs above a critical coupling parameter. It is interesting to note that the simulation studies performed by Linse and Lobaskin [48, 49] found that like-charged attraction between spheres occurs above the same critical coupling parameter that Rouzina and Bloomfield predicted for charged plates. In addition, a new theory called strong-coupling theory (SC) [53, 54] has been introduced. Using this theory, it is possible to predict the parameters required for like-charged attraction to occur. According to SC theory, like-charged attraction is expected if the Manning parameter for spheres and the coupling parameter are high enough. However, unlike infinite rods and plates, spheres in infinite dilution cannot bind a counterion, which is necessary for like-charged attraction to occur. For this reason the colloid concentration must be finite. This leads to a critical Manning parameter

that depends on colloid density [53, 54]. In all simulations in which like-charged attraction is observed, the Manning parameter is indeed above the critical value predicted by SC theory.

While previous simulation studies have focused on the effect of ion charge, here we we explore the effect of *colloid charge* on like-charged attraction using simulations of the primitive model. We investigate the transition from repulsive to attractive interactions as the colloid charge is increased as well as how the interaction changes at colloid charges well beyond this transition. Because there is a large size asymmetry between the ions and the colloidal particles, we again employ the GCA [9, 10]. However, the long-range nature of the electrostatic potential causes the GCA to become inefficient and therefore the algorithm must be modified to allow the efficient simulation of charged systems.

4.1 Simulation method

In order to understand how the GCA was extended to efficiently simulate charged systems, it is helpful to first briefly outline how the GCA works. In the GCA, cluster of particles, interacting through an arbitrary pair potential $V(r)$, are constructed in the following way. A pivot is chosen at a random point and a randomly chosen particle is point-reflected with respect to the pivot. All particles that interact with the first particle in its new or in its original position are considered for a point-reflection with respect to the same pivot. The probability that a particle is point-reflected is given by $p_{ij} = \max[1 - \exp(-\beta\Delta_{ij}), 0]$ where $\Delta_{ij} = V(|\mathbf{r}_i' - \mathbf{r}_j|) - V(|\mathbf{r}_i - \mathbf{r}_j|)$, $\mathbf{r}_i$ is the original position of the first particle, $\mathbf{r}_i'$ is the new position of the first particle, $\mathbf{r}_j$ is the position of the particle being considered for inclusion in the cluster, and $\beta = 1/k_{\mathrm{B}}T$. If a particle j is indeed added to the cluster, all other particles that interact with j in its new or in its original position and that are not already in the cluster are considered in turn. This process is thus carried out in an iterative fashion until all interacting particles have been considered. With this method, detailed balance is satisfied without the need for an acceptance criterion, making it a rejection-free algorithm; once a cluster is constructed it is always moved. Periodic boundary conditions must always be employed, in order to permit a random placement of the pivot.

4.1.1 Geometric cluster algorithm with electrostatic interactions

Since the GCA can, in general, handle any pair potential, we now consider the Coulomb interaction, given by

$$V(r_{ij}) = \frac{q_i q_j}{4\pi\varepsilon_0\varepsilon_r r_{ij}} \ , \tag{4.1}$$

for two particles with charge q_i and q_j, respectively, that are separated by a distance $r_{ij} = |\mathbf{r}_{ij}| = |\mathbf{r}_i - \mathbf{r}_j|$, where ε_0 is the permittivity of free space and ε_r is the relative dielectric constant. The total electrostatic energy of a periodic system of dimensions $L \times L \times L$ containing N charged particles is thus

$$\frac{1}{2}\sum_{\mathbf{n}}{}' \sum_{i=1}^{N}\sum_{j=1}^{N} V(|\mathbf{r}_{ij} + \mathbf{n}L|) \ , \tag{4.2}$$

where the sum over $\mathbf{n} = (n_x, n_y, n_z)$, with $n_x, n_y, n_z \in \mathbb{Z}$, runs over all periodic images of the system and the prime indicates that the term with $i = j$ is omitted for $\mathbf{n} = \mathbf{0}$. Owing to the slow decay of the electrostatic potential (4.1), Eq. (4.2) is only conditionally convergent [41]. One common method that is used to overcome this is the Ewald sum [41,42,55,56]. The Ewald sum splits the potential-energy calculation into a short-ranged contribution that is evaluated in real space and a long-range contribution that is evaluated in Fourier space. The sum is pairwise additive and the resulting pair potential is given by [42]

$$V(r_{ij}) = V_{\text{real}}(r_{ij}) + V_{\text{Fourier}}(r_{ij}) \ , \tag{4.3}$$

where

$$V_{\text{real}}(r_{ij}) = \frac{q_i q_j \text{erfc}(\alpha r_{ij})}{4\pi\varepsilon_0\varepsilon_r r_{ij}} \tag{4.4}$$

and

$$V_{\text{Fourier}}(r_{ij}) = \frac{1}{\varepsilon_0\varepsilon_r V}\sum_{k\neq 0}\frac{q_i q_j}{k^2}\exp(-k^2/4\alpha^2)\cos(\mathbf{k}\cdot\mathbf{r}_{ij}) \ . \tag{4.5}$$

We have assumed conducting boundary conditions [41, 42] and also have omitted the self-interaction correction, as it is a constant contribution that is immaterial in canonical simulations. It is possible to use the pair potential Eq. (4.3) in the GCA to construct clusters, but there are important limitations. Since the GCA considers all particles on a pairwise basis, the effect of electrostatic screening is not taken into account when constructing clusters. The unscreened electrostatic potential decays slowly, which leads to non-negligible

energy differences, Δ_{ij}, in the probability p_{ij}, even if $|\mathbf{r}_i' - \mathbf{r}_i|$ is small. Since a particle can be considered multiple times for inclusion in the cluster, the cumulative probability that it will be included is typically quite significant. This causes clusters to be constructed that frequently contain nearly all of the particles in the system. The problem is worse at lower temperatures, where the interactions are stronger, and at higher densities, where there are more interacting particles in the same volume.

In order to reduce the average cluster size, we now use the fact that the pair potential can be split into two parts in the GCA. Only the first part is used to build the cluster, whereas the second part is used to accept or reject the cluster move. Indeed, a specific variation of this was originally proposed to generalize the geometric cluster algorithm for hard spheres to arbitrary potentials, where only the hard-sphere potential is used to build a cluster, which is then accepted or rejected based on the energy difference between the new and the old configuration [57, 58]. Generally, this method leads to low acceptance ratios, as the clusters are constructed without taking into account the full interactions. However, for systems of charged particles the Ewald sum provides a natural way to split the pair potential. We use the real-space part, V_{real}, to build a cluster and subsequently consider the part of the internal energy that is evaluated in Fourier space,

$$E_{\text{Fourier}} = \frac{1}{2} \sum_{i=1}^{N} \sum_{j=1}^{N} V_{\text{Fourier}}(r_{ij}) \ , \tag{4.6}$$

to accept or reject the proposed cluster move via the standard Metropolis acceptance criterion [40–42],

$$\text{acc}(o \to n) = \min \left[1, \exp\{-\beta \left(E_{\text{Fourier}}(n) - E_{\text{Fourier}}(o)\right)\}\right] \ , \tag{4.7}$$

where o and n denote the original and the new configuration, respectively. V_{real} resembles a screened electrostatic potential and ensures that most of the relevant energy differences are taken into account during the construction of a cluster. Since the momentum-space contribution, E_{Fourier}, accounts for the long-wavelength fluctuations in the energy, which typically largely cancel out, it may be expected that a relatively high acceptance ratio can be maintained. This expectation is explored in detail in the following section.

4.1.2 Optimizing the average cluster size

One advantage of splitting the potential is the ability to adjust the screening parameter α to increase efficiency. Usually, the value of α that maximizes efficiency is given by [59–61],

$$\alpha_{\text{optimal}} = \left(\frac{\tau_R \pi^3 N}{\tau_F L^6} \right)^{\frac{1}{6}} , \tag{4.8}$$

where N is the number of particles in the system, L is the box size, τ_R is the time needed to evaluate V_{real} for one pair of particles, and τ_F is the time needed to evaluate one term in E_{Fourier}. Equation (4.8) represents the optimal α for the calculation of the total system energy, which requires $N_R \propto N^2/\alpha^3$ evaluations of V_{real} and $N_F \propto N\alpha^3$ terms in the Fourier part of the energy. However, in the GCA with a split potential, we need the energy change induced by moving a subset of all particles. For a cluster constructed by means of $V_{\text{real}}(r)$, the number of evaluations can be estimated as $N_R \propto N_C N/\alpha^3$, where N_C is the number of particles in the cluster, which in turn depends on α as well. The most efficient evaluation of the resulting change in E_{Fourier} is achieved by noting that

$$E_{\text{Fourier}} = \frac{1}{2} \sum_{k \neq 0} \frac{|\rho(\mathbf{k})|^2}{\varepsilon_0 \varepsilon_r V k^2} \exp\left(-k^2/4\alpha^2\right) , \tag{4.9}$$

where

$$|\rho(\mathbf{k})|^2 = \left[\sum_{i=1}^{N} q_i \cos(\mathbf{k} \cdot \mathbf{r}_i) \right]^2 + \left[\sum_{i=1}^{N} q_i \sin(\mathbf{k} \cdot \mathbf{r}_i) \right]^2 . \tag{4.10}$$

The values of $\cos(\mathbf{k} \cdot \mathbf{r}_i)$ and $\sin(\mathbf{k} \cdot \mathbf{r}_i)$ change only for particles that are included in the cluster. For $N_C < N/2$ it is therefore considerably more efficient to store the sums in Eq. (4.10) for all values of $\mathbf{k}$, and update the sums for the particles that belong to the cluster. In this approach, the number of terms N_F is proportional to $N_C\alpha^3$. Optimization of the parameter α is more complicated than in Eq. (4.8), since there is no simple expression for the dependence of cluster size N_C on α. However, the optimal value can be found from systematic variation of α in a number of test runs, as we will illustrate.

As an example system we choose an aqueous solution of colloidal particles with diameter 14.2 nm and charge $Q = 10e$, at a volume fraction $\phi = 0.10$. In addition, the suspension contains monovalent counterions, as well as 7.75 mM of monovalent salt. For 20 colloids in a cubic cell with linear size $L =$ 67 nm, this corresponds to 200 counterions and 2800 salt ions, where we set the hydrated ion diameter to

7.1 Å. Both colloids and ions are modeled at the level of the primitive model, i.e., with a repulsive hard core, and we use an implicit solvent model. The temperature is set to 298 K and $\varepsilon_r = 79$.

Figure 4.1(a) confirms that increasing α leads to a monotonic decrease of the size of the clusters that are constructed, owing to the decreasing range of the real-space interaction. As a result, the required computational effort ($\sim N_R$) to *construct* a cluster decreases. Initially, the number of terms N_F in the *acceptance criterion* decreases as well, but once the variation of N_C with α levels off, the increasing number of wave vectors required for sufficient accuracy in E_{Fourier} starts to dominate and slows down the simulation. As shown in Fig. 4.1(a) (open squares), for all values of α the average cluster contains a significant number of particles (although it decreases quite significantly when αL is increased from 9 to 11), and it is by no means obvious that a reasonable acceptance ratio can be maintained. Nevertheless, as illustrated in Fig. 4.2(a), the acceptance ratio lies between 40% and 75% for all $\alpha L \geq 9$. It must be noted that many of the accepted clusters are relatively small, as depicted by the solid squares in Fig. 4.1(a). This effects originates in the presence of large numbers of small ions when almost all clusters are started from such an ion. Since many small particles are fairly isolated and can be moved over larger distances without seriously disrupting a configuration, clusters containing only a few ions are accepted disproportionately often.

A important optimization of the GCA is therefore achieved by always starting the cluster construction with a large particle. This does not violate detailed balance or ergodicity [10], but permits the algorithm to focus on the species with the longest relaxation time. It also highlights another feature of the GCA, namely that it automatically ensures that the computational effort is primarily devoted to those smaller particles that affect the larger species, whereas smaller particles that are remote from any large particle (and essentially constitute a "background") are included in a cluster much less frequently. This is of particular benefit for calculations of effective interactions [17], where one aims to obtain an accurate estimate of the pair correlation function of the large species. As illustrated in Fig. 4.1(b), this approach increases the size of the constructed clusters for all $9 \leq \alpha L \leq 15$ (open squares). Importantly, also the average size of the *accepted* clusters increases very significantly, and now lies between 80 particles (for $\alpha L = 11$) and 40 particles (for $\alpha L = 15$). While there is a corresponding sharp decrease in the acceptance ratio [Fig. 4.2(b)], it remains above 10% for $\alpha L > 11$ and even exceeds 15% for $\alpha L \geq 13$. These ratios are very significant: In an unbiased Monte Carlo scheme, it would be extremely difficult to achieve acceptance ratios comparable to those shown in Fig. 4.2(b) for the simultaneous, nonlocal move of $\mathcal{O}(10)$ to $\mathcal{O}(100)$ particles. Thus,

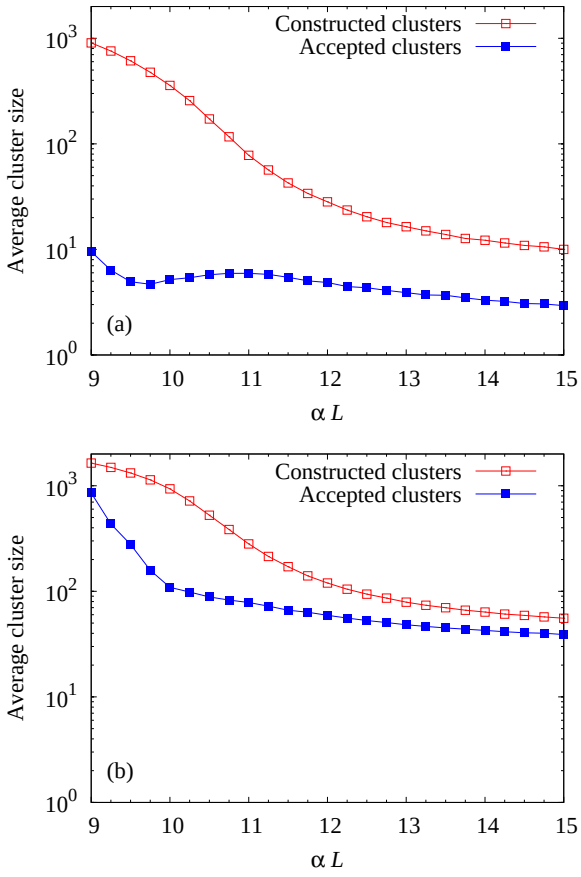

Figure 4.1: Illustration of the dependence of the average cluster size on the screening parameter αL [*cf.* Eq. (4.4)] for an example system consisting of a solution of charged colloids and monovalent salt. The colloidal particles are 20 times larger than the salt ions and carry a 10 times larger charge. The system contains a total of 20 colloids and 3000 ions. Further details are described in the text. The open squares (connected by solid lines to guide the eye) represent the average size of the clusters *proposed* by the geometric cluster algorithm. Upon increase of the screening parameter α, this cluster size decreases monotonically. The solid squares (connected by dashed lines) represent the average size of the clusters that are actually *accepted*. Panel (a) pertains to a cluster construction procedure in which the starting particle of the cluster is chosen at random from among the colloids and the ions. In this case, the average clusters become relatively small for large αL (small cutoff), since clusters will relatively often consist of isolated ions. In panel (b), the clusters are always constructed starting from a colloid. This increases the average size of both the constructed and the accepted clusters. It is noteworthy that beyond $\alpha L = 10$ the average size of the accepted clusters decreases only gradually from approximately 100 particles to approximately 40 particles. Thus, the algorithm is not particularly sensitive to the precise choice of the screening parameter. Furthermore, while the accepted clusters are systematically smaller than the constructed clusters, they still involve the nonlocal translation of a significant number of particles.

this corroborates the expectation that clusters constructed on the basis of Eq. (4.4) capture the physical structure of the fluid. The GCA is able to take into account most of the energy changes resulting from the collective move and the long-wavelength fluctuations indeed mostly cancel out. The fact that large clusters and relatively high acceptance ratios are observed for all $\alpha L \gtrsim 11$ is encouraging, as it indicates that the

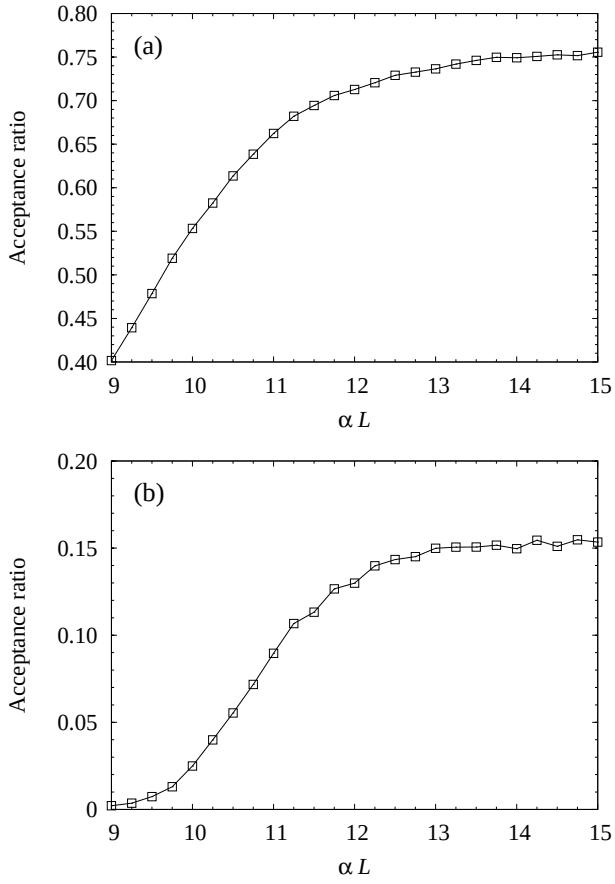

Figure 4.2: Acceptance ratio as a a function of the screening parameter αL for the system of Fig. 4.1. Panel (a) corresponds to Fig. 4.1(a), in which clusters are started from an arbitrarily chosen particle. In this case, the accepted clusters are typically rather small and the acceptance ratio is correspondingly large. If, instead, each cluster is started from a large particle, the accepted clusters are significantly larger [*cf.* Fig. 4.1(b)]. For the very large clusters constructed for $\alpha L < 10$, the acceptance ratio is very small. However, for $\alpha L > 11$, where the average size of the constructed clusters ranges between approximately 210 and 55 particles, the acceptance ratio is more than 10%. As illustrated in Fig. 4.1, even the accepted clusters involve 70 to 40 particles, which are typically translated over large separations in a cluster move.

algorithm is not particularly sensitive to the precise tuning of the screening parameter. Nevertheless, it may be favorable to make αL not too large, since larger values of α require a larger number of wave vectors n_F in the computation of the Fourier part of the internal energy.

This notion can be made more precise by considering the autocorrelation time. The optimal value of α minimizes the time required to produce an independent configuration. Since the large particles are expected to decorrelate most slowly, we compute the integrated autocorrelation time [62] of the electrostatic energy of the large particles only (thus, all ion–ion and colloid–ion interactions are excluded). Indeed, consideration of the *total* electrostatic energy may give a misleading result for the autocorrelation time,

since a significant contribution to the energy arises from the interactions among the smaller species, which decorrelate rapidly even when local algorithms are used. Figure 4.3 shows the autocorrelation time for the colloidal particles in the example system described above. For small α the autocorrelation time is large, because large clusters need to be constructed that, moreover, have a low acceptance ratio. At very large values of α, we anticipate the configuration to evolve slowly because the clusters are small, and the evaluation of the change in E_{Fourier} involves a large number of wave vectors. These considerations are partly borne out in the graphs. While there is a very strong decay of the autocorrelation time when αL is increased from 9 to 12, it remains fairly constant for $\alpha L \gtrsim 12$. This indicates that the increased computational cost of evaluating the Fourier part of the internal energy and the (weak) decrease in cluster size are compensated by the increasing acceptance rate (possibly, the variation in the nature of the clusters that are constructed also enhances the decorrelation of subsequent configurations). The constant autocorrelation time shows that efficient simulations are possible over a range of values of the screening parameter. Indeed, systems with a size asymmetry of 20 would be almost infeasible without employing the GCA, as will be demonstrated in Sec. 4.1.3. There is no strong qualitative difference in the dependence on α for a cluster construction procedure in which one starts with an arbitrary particle [Fig. 4.3(a)] and for a procedure in which one always starts with a large particle [Fig. 4.3(b)]. Interestingly, for the example system studied here the approach of Fig. 4.1(a), which seems less appealing in terms of the average size of the accepted clusters, is *more efficient* in decorrelating the colloids than the approach of Fig. 4.1(b), even though the latter explicitly targets the large particles. It must be noted that this observation may be different for systems with different number ratios of large and small particles. Likewise, the range of optimal values of αL is system dependent. In fact, to maintain a constant cluster size when L is varied requires a constant real-space cutoff, i.e., a constant α rather than a constant αL. However, there is no universal formula for the optimal value of α, because the dependence of the cluster size, the acceptance rate, and the speed of the simulation on α are dependent on the specific system parameters.

4.1.3 Efficiency comparison

Size-asymmetric mixtures, such as charged colloids suspended in an ionic solution, are natural candidates for the application of the GCA for charged systems. Here, we consider such a solution to perform a systematic efficiency comparison of the GCA *versus* a standard molecular dynamics (MD) simulation, as a

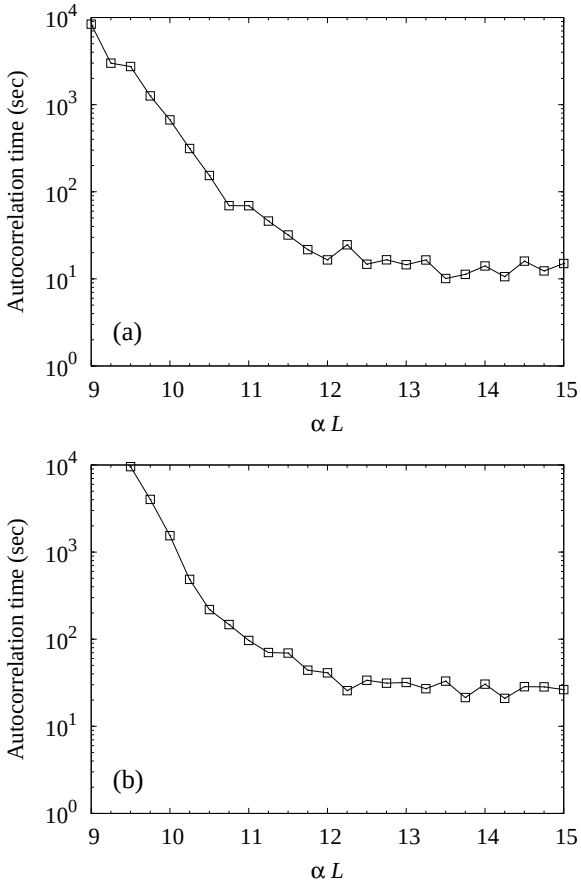

Figure 4.3: Autocorrelation time for the electrostatic energy of 20 charged colloidal particles in a solution with 200 counterions and 7.75 mM of monovalent salt (2800 salt ions). Panels (a) and (b) correspond to the panels in Figs. 4.1 and 4.2, respectively. All times are measured in seconds of CPU time. The autocorrelation time decreases rapidly as the screening parameter is increased from $\alpha L = 9$ to $\alpha L = 12$ and then remains approximately constant until $\alpha L = 15$. For the model system studied here, the optimal autocorrelation time in panel (a), in which each cluster is started with a randomly chosen particle, is approximately twice smaller than the optimal autocorrelation time in panel (b), in which each cluster is started with a colloidal particle.

function of size ratio between the colloids and the ions. The system is kept at a temperature of 298 K, with the solvent (water) modeled implicitly as a dielectric medium with $\varepsilon_r = 79$. The cubic cell with volume V contains 10 large particles (colloids) with a variable radius R_l and positive charge Q_l, at a fixed volume fraction $\phi_l = 0.01$. Both the N_c (negatively charged) counterions of the colloids and the additional $N^-_{\rm salt} + N^+_{\rm salt}$ salt ions are spherical particles with a (hydrated) diameter equal to the Bjerrum length, i.e., a radius $R_s = 3.55$ Å. All ions are monovalent. As the size of the colloids is increased, their charge increases linearly with the radius. This keeps the interaction strength at contact between the colloids and the ions from increasing, and therefore any change in the cluster size results only from the increasing size ratio and

not from stronger interactions. The total ion volume fraction $\phi_s = \frac{4}{3}\pi R_s^3(N_c + N_s^- + N_s^+)/V$ is fixed at $\phi_s = 0.01$. In order to facilitate comparison to MD calculations, we adopt a smooth excluded-volume potential,

$$V_{\mathrm{ex}}(r_{ij}) = k_{\mathrm{B}}T \left(\frac{R_i + R_j}{r_{ij}} \right)^{12} , \tag{4.11}$$

such that the cluster construction is based upon the sum of $V_{\mathrm{ex}}(r)$ and $V_{\mathrm{real}}(r)$. Table 4.1 lists some properties for the systems investigated here. The MD simulations are carried out with a modified version of LAMMPS [63]. The NVT ensemble is used, in which the temperature is controlled by a Nosé–Hoover thermostat. Figure 4.4 presents the radial distribution functions (RDF) for ion–ion, ion–colloid and colloid–colloid pairs with $R_l/R_s = 2$. There is excellent agreement between the MD and the GCA results.

Table 4.1: Properties of the systems investigated for the efficiency comparison between the GCA and a standard molecular dynamics simulation. R_l/R_s is the size ratio between large particles (colloids) and small particles (ions), Q_l is the colloidal charge, N_c is the number of counterions, N_s^- and N_s^+ are the number of negative and positive salt ions, respectively, and $L/(2R_s)$ is the linear system size in units of ion diameter. All systems contain 10 large particles.

R_l/R_s	Q_l	N_c	N_{salt}^-	N_{salt}^+	$L/(2R_s)$
1	$1e$	10	0	0	8.06
2	$2e$	20	30	30	16.12
4	$4e$	40	300	300	32.24
6	$6e$	60	1050	1050	48.36
8	$8e$	80	2520	2520	64.48
10	$10e$	100	4950	4950	80.60

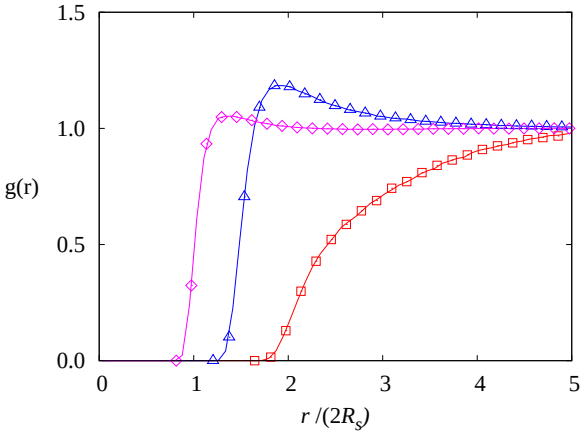

Figure 4.4: Comparison between MD (solid lines) and GCA (symbols) results for radial distribution functions in the system described in Table 4.1, with $R_l/R_s = 2$. Diamonds, triangles, and squares represent ion–ion, colloid–ion, and colloid–colloid correlations, respectively. Since this graph is only intended to demonstrate the agreement between the GCA and MD results, no distinction is made between positive and negative ions.

As in Fig. 4.3, we employ the integrated autocorrelation time (expressed in units of CPU time) of the total interaction energy of the *large* particles to determine the rate at which independent configurations can be produced. Variation of the size asymmetry R_l/R_s requires choices to be made about other system parameters. If the total number of particles is kept constant, there is a decrease in ϕ_s with increasing size asymmetry, which will diminish "jamming" effects. On the other hand, if ϕ_s is kept constant, there is a rapid increase in the total number of particles as R_l/R_s is increased. Since the Ewald summation scales superlinearly with total particle number, this results in increasing autocorrelation times even after normalization per particle. Nevertheless, this provides a stringent test of the GCA, since the optimal tuning parameter (Fig. 4.3) will generally not coincide with the value of α that yields $\mathbb{O}(N^{3/2})$ scaling, Eq. (4.8).

We first consider the implementation of the GCA in which each cluster is started with an arbitrary particle. As shown in Fig. 4.5, in the absence of size asymmetry ($R_l/R_s = 1$) this method (solid squares) requires almost the same computational effort as a standard molecular dynamics simulation (solid triangles). However, when the size of the large particles is increased the autocorrelation time per particle in the MD simulation increases rapidly. This reflects the combined effect of the trapping of large particles by ions, reducing the diffusion rate of the large particles, and the slowdown ($\propto \sqrt{N}$) in the Ewald summation. The autocorrelation times of the GCA demonstrate that the nonlocal moves effectively overcome the trapping of large particles, resulting in a very weak increase of the autocorrelation time with size asymmetry. The increase for $R_l/R_s = 8$ and $R_l/R_s = 10$ mostly reflects increased computational effort because of an increase in the tuning parameter α (and a consequent increase in the number of wave vectors). For completeness, we also investigate the autocorrelation time for the GCA in which each cluster is started with a large particle (open squares in Fig. 4.5). This makes it possible to explicitly focus a larger fraction of the computational effort on moving the large particles and results in even smaller autocorrelation times for the range of parameters depicted here. However, the difference with the solid symbols decreases at larger size ratios. This occurs because clusters are larger when starting with only large particles and therefore take more time to construct. As R_l/R_s is increased, these clusters increase in size since the large particles occupy more volume and therefore interact with more small particles. Indeed, this observation is consistent with the observation in Fig. 4.3 that starting with a large particle is actually *disadvantageous* for $R_l/R_s = 20$.

In order to isolate the effect of the Ewald summation on the decrease in efficiency, we have also performed MD simulations in which the Ewald summation is performed via the particle-particle particle-mesh

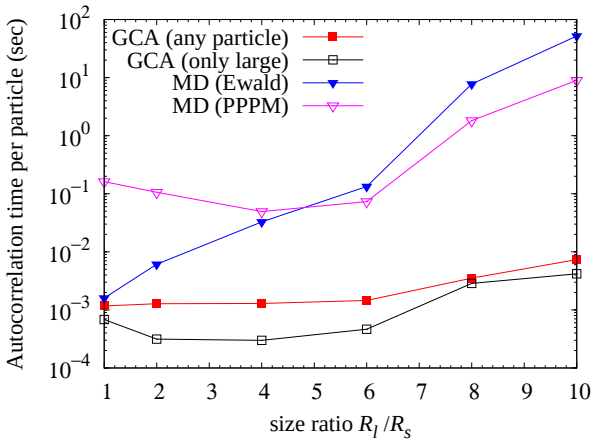

Figure 4.5: Systematic efficiency comparison of the GCA and molecular dynamics simulations, for an ionic solution containing charged colloids. The size asymmetry R_l/R_s is varied while keeping both the colloid number and volume fraction ϕ_l, and the ion volume fraction ϕ_s fixed. The MD simulations are performed both with a conventional Ewald summation (closed triangles) and with the particle–particle particle–mesh method (PPPM, open triangles) with a relative accuracy of 10^{-5}, the same as for the GCA. The graph shows the integrated autocorrelation time (in seconds of CPU time) computed for the interaction energy of the colloids, which is a measure for the time required to decorrelate the slowest species. Although the PPPM method outperforms the Ewald summation for a sufficiently large number of particles (large R_l/R_s), it still displays a significant slow-down with increasing size asymmetry, owing to jamming effects. By contrast, the GCA (squares)—which employs conventional Ewald summation—can create independent configurations at a much higher rate than even the fastest MD approach for all size ratios $R_l/R_s > 1$. Open squares refer to the GCA in which each cluster is started with a colloid, whereas closed squares represent the GCA in which each cluster is started with an arbitrary particle (colloid or ion).

(PPPM) method [64]. This decreases the computational efforts to $\mathcal{O}(N \log N)$, i.e., the time per particle increases only logarithmically with the total number of particles. Since the PPPM method involves considerable computational overhead it only outperforms a regular Ewald summation for a sufficiently large [$\mathcal{O}(10^3)$] number of particles. The results are included in Fig. 4.5 (open triangles). For small R_l/R_s the PPPM method is much slower than conventional Ewald summation, which simply results from the small number of particles that we employ. However, for $R_l/R_s \geq 6$ the PPPM method outperforms the Ewald summation and the increasing autocorrelation time per particle for $R_l/R_s = 8$ and $R_l/R_s = 10$ now almost completely reflects the effect of jamming. Nevertheless, despite the fact that the GCA does *not* have the advantage of a fast electrostatics calculation, it remains much more efficient for all parameter choices investigated here.

4.2 Critical colloid charge

Using this new algorithm, we now investigate how the colloidal interactions change as the colloid charge is increased in two different systems. In one system, $\varepsilon_r = 28$ and $\phi_l = 0.01$ and in the other, $\varepsilon_r = 78.4$ and $\phi_l = 0.02$. For both systems, the temperature is set to 298 K and the colloids have a hard-sphere diameter ranging from 1.2 nm to 10 nm. For each colloid size, Z is varied and there are enough counterions with a charge valency of $q = 3$ and a hard-sphere diameter of 4 Å to neutralize the system. We observe finite-size effects for systems with up to 40 colloids, which is consistent with earlier simulations of similar systems [49] and we use at least 60 colloids. In the simulations, the potential of mean force, $W(r)$, is determined from the pair correlation function, $g(r)$, through the following relation,

$$W(r) = -\frac{\log[g(r)]}{k_{\mathrm{B}}T}\,, \tag{4.12}$$

where k_{B} is the Boltzmann constant. Figure 4.6 shows a representative example of how $W(r)$ changes as Z is increased in a system with $\sigma_l = 4$ nm and $\varepsilon_r = 78.4$. When $Z = 10$, $W(r)$ is purely repulsive, however increasing the colloid charge to $Z = 15$ causes an attractive minimum to develop in $W(r)$. The same qualitative behavior is observed for all values of σ_l investigated and for each σ_l the minimum colloid charge which results in an attractive minimum in $W(r)$ is determined. We refer to this value of the colloid charge, Z_c, as the critical colloid charge and, as shown in Fig. 4.7, Z_c increases with σ_l.

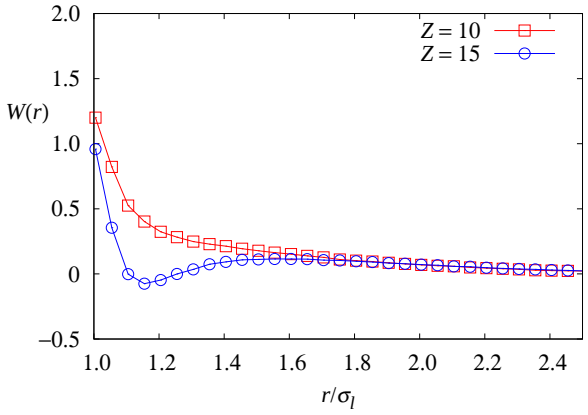

Figure 4.6: Potential of mean force, $W(r)$, for a system with $\sigma_l = 4$ nm and $\varepsilon_r = 78.4$ for two different values of Z. When $Z = 10$ (squares), $W(r)$ is purely repulsive, however, increasing the colloid charge to $Z = 15$ (circles) results in an attractive minimum in $W(r)$. From this we determine that $Z_c \approx 15$ is the value of the critical colloid charge.

Many properties of charged systems are controlled by a number of factors including the colloid size and charge, the counterion size and charge, and the Bjerrum length, $\ell_B = e^2/(4\pi\varepsilon_0\varepsilon_r k_B T)$, where, e is the elementary charge, which is the distance between two counterions at which the interaction energy equals the thermal energy. It is convenient to define a unitless parameter combining these factors which can be used to make predictions about the system behavior. One choice for a unitless parameter is the coupling parameter Γ,

$$\Gamma = \sqrt{\frac{Zq^3\ell_B^2}{\pi(\sigma_l + \sigma_s)^2}} \,. \tag{4.13}$$

This parameter represents the ratio of ℓ_B, which is a length scale associated with the counterion-counterion interaction, and the Gouy–Chapman length, μ, which is the distance at which the interaction energy between a single counterion and a colloid equals the thermal energy. For spheres this can be written as

$$\mu = \frac{(\sigma_l + \sigma)^2}{2Zq\ell_B} \,. \tag{4.14}$$

Based on an investigation of infinite plates, Rouzina and Bloomfield predicted that like-charged attraction occurs at values of Γ greater than $\Gamma_c = 2$ [52]. Using this value, the critical colloid charge, $Z_{c,\Gamma}$, can be calculated as

$$Z_{c,\Gamma} = \frac{\Gamma_c^2\pi\sigma_s^2(\frac{\sigma_l}{\sigma_s} + 1)^2}{q^3\ell_B^2} \,. \tag{4.15}$$

The Manning parameter, ξ, is also a unitless parameter which, for spheres, reads

$$\xi = \frac{Zq\ell_B}{\sigma_l + \sigma_s} \tag{4.16}$$

and can be expressed as the ratio of the distance of closest approach between a colloid and a counterion, and μ. Using SC theory, Netz *et al.* predicted that for like-charged attraction to occur, in addition to the criterion $\Gamma > \Gamma_c$, the Manning parameter must also be above a critical value, $\xi_c = 3.3$, for systems with colloid densities similar to what we investigate [53, 54]. Using this value it is possible to determine the critical colloid charge,

$$Z_{c,\xi} = \frac{\xi_c\sigma_s(\frac{\sigma_l}{\sigma_s} + 1)}{q\ell_B} \,. \tag{4.17}$$

While SC theory treats Γ and ξ as independent parameters, they are actually closely related. By dividing

Eq. (4.13) by Eq. (4.16) we see that

$$\Gamma = \xi\sqrt{\frac{q}{\pi Z}} \tag{4.18}$$

and the only way to independently vary these parameters is by changing the ratio q/Z. We explore this by varying Z, keeping q constant.

The critical colloid charge calculated from ξ_c and from Γ_c differ not only in their numerical values, but also in their dependence on σ_l. Figure 4.7 shows $Z_{c,\xi}$ and $Z_{c,\Gamma}$ as a function of σ_l/σ_s along with the values obtained from the simulations. When $\varepsilon_r = 28$, there is an appreciable region where $Z_{c,\xi} > Z_{c,\Gamma}$. In this region, the simulation points follow a straight line and lie above $Z_{c,\Gamma}$. The value of ξ_c was determined in the limit $\Gamma \to \infty$, which may account for the lack of a better quantitative agreement of the numerical data with $Z_{c,\xi}$. At size ratios where $Z_{c,\xi} < Z_{c,\Gamma}$, the simulation points increase quadratically and closely follow the values of the critical charge predicted in Eq. (4.15). This confirms that both ξ and Γ must be above their critical values for like-charged attraction to occur. However, for most experimentally relevant systems, if $\Gamma > \Gamma_c$, then $\xi > \xi_c$. This can be seen in the inset of Fig. 4.7 where $\varepsilon_r = 78.4$.

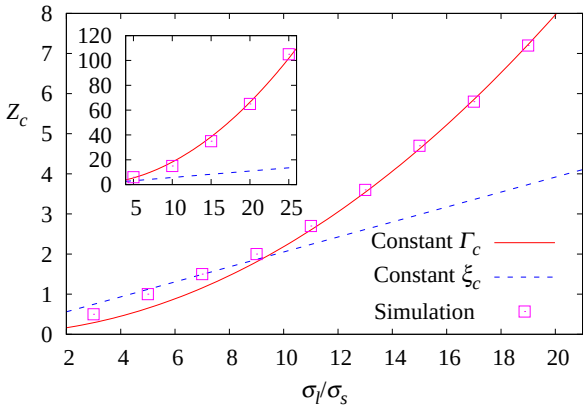

Figure 4.7: Critical colloid charge, Z_c, as a function of size ratio, σ_l/σ_s for $\varepsilon_r = 28$ and $\varepsilon_r = 78.4$ in the inset. The solid red curve is at a constant coupling parameter, $\Gamma = 2$, which is predicted by Rouzina and Bloomfield. The dashed blue curve is at a constant Manning parameter, $\xi = 3.3$, which is predicted by SC theory, and the squares are the critical colloid charge determined from simulations; the error bars are smaller than the symbol size. The simulation results are in good agreement with the prediction that both ξ and Γ must be above their critical values for attraction to occur.

4.3 Effect of increasing colloid charge

In addition to determining the onset of like-charged attraction, we also investigate the behavior of $W(r)$ for higher colloid charges. For a fixed diameter $\sigma_l = 8$ nm, we vary the colloid charge from $Z = 60$ to 120 keeping the other system parameters the same as before. As shown in Fig. 4.8, the magnitude of the attraction increases linearly with colloid charge. Interestingly, the height of the repulsive barrier does not increase despite the fact the strength of the direct colloid–colloid repulsion increases. The barrier height for this system with $\sigma_l = 8$ nm is larger than for the system with $\sigma_l = 4$ nm, shown in Fig. 4.6. This trend of increasing barrier height with σ_l is observed for all the systems investigated.

The observation that the barrier height does not increase with increasing Z is similar to results obtained from charge renormalization calculations [65–67]. The concept of charge renormalization is that, at large enough distances, the effective potential between charged colloids, $V_{\text{eff}}(r)$, is of the Yukawa form,

$$V_{\text{eff}}(r) = \frac{(Ze)^2}{\varepsilon r} \exp[-\kappa r] \,, \tag{4.19}$$

where, κ is the inverse Debye screening length, but with renormalized values for Z and κ [65]. Using Alexander's prescription for charge renormalization [66] as well as other methods [67], it is found that the renormalized value for the charge reaches a saturation value beyond which it is independent of the bare charge. Calculations of the no-salt case show that this saturation value only depends on the colloid size and the Bjerrum length [66, 67]. These observations are in agreement with our observations that beyond a separation of $r = 1.3\sigma_l$, $W(r)$ does not depend on the value of the colloid charge.

4.4 Summary and conclusions

In conclusion, in this chapter we have investigated the effect of colloid charge on the effective interactions of charged colloids in the presence of multivalent counterions. We determined the critical charge for like-charged attraction as a function of colloid diameter. Our findings support the prediction that like-charged attraction occurs if both the coupling parameter $\Gamma > 2$ and the Manning parameter $\xi > 3.3$. By examining higher colloid charges we found that the strength of the attraction increases linearly with increasing Z. However, the height of the repulsive barrier does not increase with increasing Z, which is similar to results seen in charge renormalization calculations [65–67].

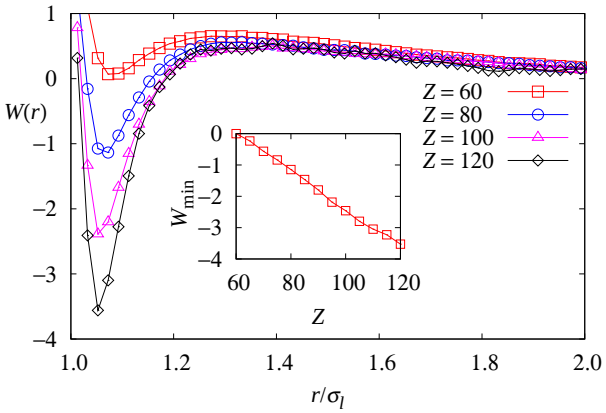

Figure 4.8: Potential of mean force, $W(r)$, for a system with $\sigma_l = 8$ nm and $\varepsilon_r = 78.4$ for different values of Z. The depth of the attractive minimum increases linearly with Z as can be seen in the inset. There is also a weak repulsive barrier in $W(r)$ which is insensitive to the value of Z. This repulsive barrier is higher than the barrier seen with the smaller colloids shown in Fig. 4.6 and we observe this trend for all the systems we investigated. These observations are similar to the results obtained from charge renormalization calculations [65–67].

Owing to the large size ratios between the colloids and the counterions, conventional MD or MC simulations could not be used. For this reason we developed a new simulation method based on the GCA, which allows for the efficient simulation of charged systems with large size ratios. For the system we investigated, finite-size effects rule out freezing the colloids at different separations and measuring the force as has been done before [46,47,51]. There are some caveats to our simulation method, though. As the interactions in the system become stronger, the simulations become less efficient and more sensitive to the value of α, which controls the real-space cutoff. An alternative simulation method which is capable of simulating systems similar to what we investigate here is the algorithm proposed by Lobaskin and Linse [68, 69], which performs well when there is a strong binding of the ions to the colloids. On the other hand, our new algorithm performs best when the ions are dispersed evenly in the solution, yet remains efficient for strongly coupled systems, and can therefore be used to study a wide range of charged colloid systems.

CHAPTER 5

CRYSTAL PHASES OF VIRUS PARTICLES

Virus particles offer an interesting system for the study of colloidal interactions. One advantage of virus particles is that it is easy to produce large quantities of monodisperse particles. Also, due to their surface protein coat, they have a non-uniform surface charge distribution which can be manipulated by altering the RNA of the virus particles. This allows the investigation of spherical particles with an anisotropic surface charge distribution in a well-controlled system.

An anisotropic surface charge distribution leads to an anisotropic interaction between virus particles which can alter their phase behavior, resulting in different crystal structures than seen for particles with isotropic interactions [70]. Recent experiments performed by Gerard Wong and Nathan Schmidt [71] have investigated this using small-angle x-ray scattering to determine the crystal structures formed by the Qβ and MS-2 virus particles. In these experiments, the virus particles were in solution with additional salt and non-adsorbing polymer and a variety of phases were observed by varying the salt conditions and the polymer size and concentration. Specifically, for Qβ with 10 kDa polyethylene glycol (PEG), which has a radius of gyration $R_g \approx 4.8$ nm in 100 mM $CaCl_2$, a transition from HCP to FCC is observed as the polymer concentration is increased, as shown in Fig. 5.1. This transition, however, is not observed for the MS-2 virus under the same conditions, where the only crystal structure observed is FCC [71].

The difference between FCC and HCP is well understood for systems with short-ranged isotropic interactions [43, 72–74], however, less is known about the effect of anisotropic interactions. Because Qβ and MS-2 are very similar and differ primarily in their surfaces charges, we can gain insight into this effect by investigating these particles. It is therefore the goal of this chapter to understand why an HCP phase is observed for Qβ and not for MS-2 using computer simulations and also to understand the transition from HCP to FCC in Qβ. A detailed model of the virus particles is developed which takes into account the surface charge distribution. Salt is included explicitly using grand-canonical Monte Carlo to account for the partitioning of the salt between the crystal and aqueous phases. We measure the osmotic pressure to determine

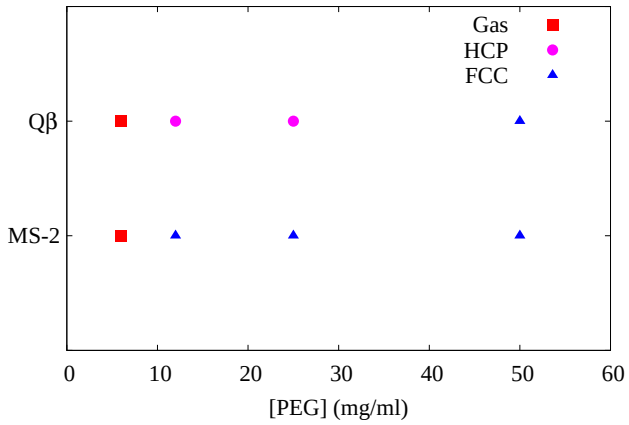

Figure 5.1: Crystal phases formed by Qβ and MS-2 as the concentration of 10 kDa PEG is increased in the presence of 100 mM $CaCl_2$. For Qβ, there is a transition from HCP to FCC as the PEG concentration is increased from 25 mg/ml to 50 mg/ml. For MS-2, only the FCC crystal structure is observed.

the stability of different crystal phases and then, using thermodynamic integration, determine how the free energy changes as the separation between the virus particles is increased. We find that beyond the stable separation there is a free energy barrier, similar to what we observed in Chapter 4 for the pair potential between like-charged colloids.

5.1 Simulation details

To study this system, we first develop a model of the virus particles which is tractable in simulations. This model must capture the essential features of the virus particles, yet be coarse-grained enough to allow for efficient simulations. We start with the atomic coordinates for the Qβ and MS-2 virus particles, which were obtained from x-ray crystallography measurements at 3.5 Å resolution [75–77]. Next, the charged state of each amino acid is determined using PDB2PQR [78, 79] and PROPKA [80]. In this program, the charge is determined from the pK_a of the amino acid, the local environment surrounding each amino acid, and the pH of the solution, which was measured to be 6.5 in the experimental system. We find that there are about 4000 charged amino acids with roughly 20,000 left uncharged.

Even including only the charged amino acids in the model would still be prohibitive to study this system, and we therefore further coarse-grain by spatially averaging the surface charges. We choose 120 points on the surface of a sphere with icosahedral symmetry [81], which matches the symmetry of the virus particles. We then add the charge of each amino acid to the nearest of these 120 points. This is depicted in Fig. 5.2.

Since the protein coat has a net positive charge, all the 120 sites are positive with 60 sites carrying a charge $+1e$ and 60 a charge $+2e$, where e is the elementary charge. The RNA is accounted for by a point charge at the center of the virus particle with a charge of $-240e$, which gives the virus particle a net charge of $-60e$, in good agreement with electrophoresis measurements [82, 83].

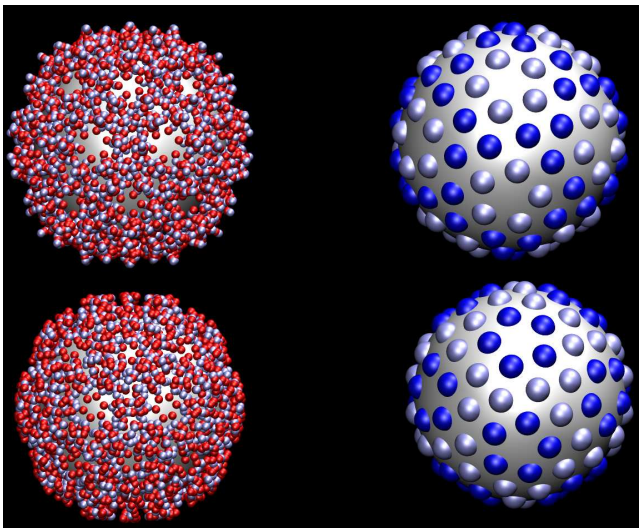

Figure 5.2: The top left panel shows the 4500 charged amino acids of Qβ with $-1e$ charges colored red and $+1e$ colored light blue. The top right is the 120-site model for Qβ. All the sites are positive, with the $+2e$ sites colored dark blue. The lower left panel shows shows the 3780 charged amino acids of MS-2 with the 120-site model shown in the lower right panel.

To facilitate the pressure computation in the simulations, we use soft potentials to model the excluded volume of the virus particles and the salt ions. The ion–ion potential is given by

$$\frac{V(r)}{k_{\mathrm{B}}T} = \left(\frac{\sigma_{\mathrm{ion}}}{r}\right)^{12} , \tag{5.1}$$

where $\sigma_{\mathrm{ion}} = 7$ Å, corresponding to a hydrated ion diameter [15]. For the interaction between an ion and a virus particle, we use a modified Lennard-Jones potential of the form

$$V(r) = 4\varepsilon\left[\left(\frac{\sigma}{r-\Delta}\right)^{12} - \left(\frac{\sigma}{r-\Delta}\right)^{6}\right] + \varepsilon , \tag{5.2}$$

where $\varepsilon = k_{\mathrm{B}}T$, $\sigma = 1$ nm and $\Delta = 12.08$ nm. The potential is cut off at $r = 2^{1/6}\sigma + \Delta$, resulting in a purely repulsive potential.

Charged interactions are calculated using the Ewald sum [41, 42, 55, 56] as in Chapter 4 and water is

represented as a homogeneous dielectric medium, with relative dielectric constant $\varepsilon_r = 80$. The temperature is set to $T = 298$ K, which results in a Bjerrum length of $\ell_B = 7$ Å.

The effect of polymer on the virus interactions is included through the Asakura–Oosawa depletion potential [26], V_{AO}, between virus particles with radius R_{virus} given by

$$V_{AO} = -k_B T \phi_p \left(d^3 - \frac{3rd^2}{4R_g} + \frac{r^3}{16R_g^3} \right) , \tag{5.3}$$

for $2R_{virus} < r < 2(R_{virus} + R_g)$ and 0 elsewhere, where ϕ_p is the polymer volume fraction, R_g is the polymer radius of gyration, and $d = R_{virus}/R_g$.

We place 32 virus particles on the lattice points of either an FCC or an HCP crystal in a periodically replicated simulation box. A cubic box is used for the FCC crystal and a rectangular box is used for the HCP crystal. They are not allowed to move from these points, however they are allowed to rotate. The salt is included using a grand-canonical Monte Carlo scheme in which the chemical potential is fixed and the number of particles fluctuates. To maintain electroneutrality, we insert or delete neutral groups of ions and since we are interested in $CaCl_2$, a group consists of two ions with charge $-1e$, representing the chlorine, and one ion with charge $+2e$ to represent the calcium ion. Adopting the approach used by Valleau and Cohen [84], we define a chemical potential μ for the neutral group which we set such that the salt is in chemical equilibrium with a bulk salt solution at a given concentration. The chemical potential is then determined by a number of grand-canonical simulations containing only salt where we set μ and measure the average concentration. By fitting the values of μ and the resulting concentrations to a line, we can readily find a target salt concentration. We use this method to determine a target salt concentration of 100 mM, matching the experimental conditions with a resulting value of $\mu = -7.815\ k_B T$, shown in Fig. 5.3. In the subsequent simulations containing virus particles, we choose randomly between insertions and deletions, and virus rotations. The acceptance rate for grand-canonical moves is close to 1% and these are performed on average 10 times more often than virus rotations. Virus particles are rotated by at most 18^0 about an arbitrary axis with an acceptance rate of 3%.

The stability of the crystal is determined by mechanical equilibrium in which the osmotic pressure of the aqueous phase, Π_{bulk}, balances the osmotic pressure of crystal phase, $\Pi_{crystal}$. The pressure is determined

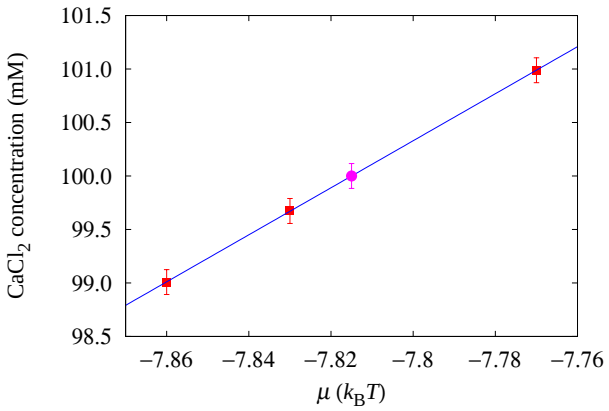

Figure 5.3: $CaCl_2$ concentration as a function of chemical potential. A linear fit to the data points (solid squares) is used to obtain the chemical potential that yields a concentration of 100 mM. This value ($\mu = -7.815\ k_{rmB}T$, circle) is then used in the simulations of the actual virus system.

for both phases by applying the virial theorem, which gives the virial tensor as [85]

$$w_{\alpha\beta} = \frac{1}{2V}\left\langle \sum_i \sum_j \sum_{\mathbf{n}}{}' (\mathbf{R}_{c(i)} - \mathbf{R}_{c(j).\mathbf{n}})_\alpha (\mathbf{F}_{ij})_\beta \right\rangle , \tag{5.4}$$

where i and j index the N interaction sites of the system, $c(i)$ gives the index of the molecule to which i belongs, $\mathbf{n}$ denotes a vector pointing from the central cell to a periodic copy, α and β are tensor indices, w is the virial tensor, V is the volume of the system, $\mathbf{R}_{k.\mathbf{n}}$ is the position of the periodic copy of molecule k reached by $\mathbf{n}$, and $\mathbf{F}_{ij}$ is the force exerted by site i on site j. The prime indicates omission of terms with $c(i) = c(j)$ if $\mathbf{n} = \mathbf{0}$, so that intramolecular forces do not contribute to the virial.

The pressure is obtained as one third of the trace of the virial tensor, plus a kinetic contribution $\rho k_B T$, where ρ is the overall density. However, since the virus particles are held fixed during the simulation, they do not contribute to the kinetic term of the pressure. Also, the forces arising from the depletion potential between the virus particles do not influence the evolution of the system and therefore do not need to be computed during the simulation, but can instead be added in later. In this way we can determine the total pressure resulting from a number of different polymer sizes and concentrations from a single simulation.

We determine Π_{crystal} for a number of different lattice spacings, with the nearest-neighbor virus separations ranging from 25.6 nm to 30.0 nm, where a separate simulation is performed for each separation. Π_{bulk} is determined from a single grand-canonical Monte Carlo simulation only including salt at a chemical potential of $\mu = -7.815\ k_B T$. The total osmotic pressure is then given by $\Pi = \Pi_{\text{crystal}} - \Pi_{\text{bulk}}$, where we

have adopted the convention of treating the water as a solvent with the virus and salt solutes defining the osmotic pressure. In this approximation, the effect of the water is accounted for by the relative dielectric permittivity, ε_r, thus the pressure obtained from the virial corresponds directly to the osmotic pressure of the solute [86]. Recalling the thermodynamic definition of pressure,

$$\Pi = -\left(\frac{\partial F}{\partial V}\right)_T \ , \tag{5.5}$$

we see that stability occurs when $\Pi = 0$ and $\partial\Pi/\partial V < 0$, which describes a minimum in the free energy F. A similar approach has been used to study the stability of bundles of rod-like polyelectrolytes condensed via counterions [87, 88].

5.2 Results

We first investigate the osmotic pressure in the absence of polymer at a bulk salt concentration of 100 mM for Qβ and MS-2. As shown in Fig 5.4, for Qβ both FCC and HCP are stable at a separation of 25.7 nm, with closer separations dominated by excluded-volume interactions. At separations larger than 26.2 nm, the pressure becomes positive, indicating a repulsive barrier which precedes the stable separation. The same behavior is also seen for MS-2 in Fig 5.5.

This barrier is investigated in more detail by considering the free energy. It is possible to compute the difference in Helmholtz free energy per virus particle, Δf, between two systems at different separations by integrating Eq. (5.5),

$$\Delta f = f_1 - f_0 = -\frac{1}{32}\int_{V_0}^{V_1} \Pi(V)\mathrm{d}V \ , \tag{5.6}$$

where V_0 and V_1 are the initial and final volumes of the simulation box containing 32 virus particles (which results in the factor $1/32$). For Qβ we see that the HCP structure has a lower free energy barrier than FCC, shown in the inset of Fig. 5.4. This difference in barrier height is due primarily to the differences between the pressures at separations beyond 27.0 nm. Although these differences are small, they are statistically significant and their accumulation leads the observed difference in barrier heights of close to 1 $K_\mathrm{B}T$. For MS-2 the difference in barrier height is smaller, within statistical error, as seen in the inset of Fig. 5.5.

Adding polymer results in an effective attraction between the virus particles and will therefore act to reduce the pressure. We investigate this effect by determining the pressure contribution from a polymer

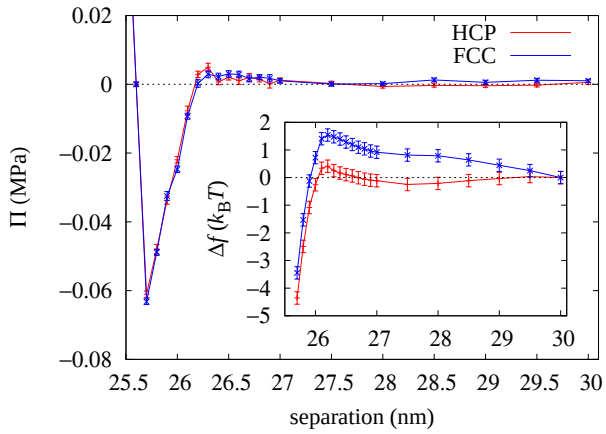

Figure 5.4: Osmotic pressure, Π, as a function of nearest-neighbor virus spacing for HCP and FCC crystal structures of the Qβ virus. Both HCP and FCC are stable at a separation of 25.7 nm. At larger separations, Π is positive, indicating a barrier to the stable separation. The free energy difference, Δf, as a function of nearest-neighbor virus spacing for the HCP and FCC crystal structures is shown in the inset. HCP has a smaller barrier height.

with $R_g = 4$ nm at volume fraction of 1.1 where the volume of a single polymer is given by $4\pi R_g^3/3$. This corresponds to 10 kDa PEG at 50 mg/ml, where the experiments observe a transition from HCP to FCC for Qβ. At this concentration the polymer coils will overlap; however, in this regime the depletion potential is still well described by Eq. (5.3) [29]. We show the resulting pressure for Qβ in Fig. 5.6. In this case, the pressure is below zero beyond the stable separation of 25.6 nm and there is no longer a free-energy barrier for either HCP or FCC structures for this polymer size and concentration, as shown in the inset of Fig. 5.6. Similar behavior is observed for MS-2, as seen in Fig. 5.7.

The absolute free energies of the HCP and FCC phases cannot be compared because at the largest separation the virus particles are still interacting with each other and therefore cannot be equated with a reference state of known free energy. The barrier heights can be compared though, and give an indication of the activation energy to form a given crystal structure, even though we only consider a single activation pathway. For Qβ with no polymer, or at low polymer concentrations, the HCP structure has a lower barrier height and is more kinetically favorable to form than an FCC crystal, which is consistent with the experimental observation of an HCP phase under these conditions. At higher polymer concentrations, these barriers are no longer present. If neither state has a kinetic barrier, the system will form the structure with the lowest absolute free energy, which we assume to be FCC, as is the case for particles with only short-ranged interactions [43, 72–74], though we are not able to determine if this is true from these simulations. For MS-2 with no added polymer, the barrier heights are very similar, within statistical error. Since the activation energies

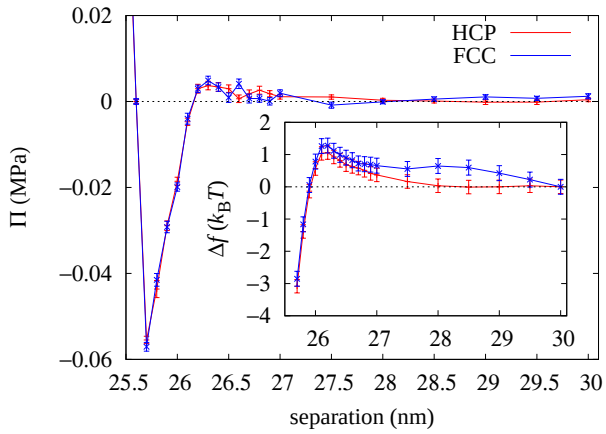

Figure 5.5: Osmotic pressure, Π, as a function of nearest-neighbor virus spacing for HCP and FCC crystal structures of the MS-2 virus. Both HCP and FCC are stable at a separation of 25.7 nm. At larger separations, Π is positive, indicating a barrier to the stable separation. The free energy difference, Δf, as a function of nearest-neighbor virus spacing for the HCP and FCC crystal structures is shown in the inset. The difference in barrier height is smaller than the statistical error.

are comparable, we expect the system to form the state with the lowest absolute free energy, which again we assume to be FCC. Reducing the barrier heights by adding polymer would not change the crystal structure observed.

5.3 Summary and conclusions

In conclusion, we have studied the phase behavior of the Qβ and MS-2 virus particles in solution with 100 mM $CaCl_2$ salt and non-adsorbing polymer. Using a coarse-grained model of the virus particles, which nevertheless provides a faithful representation of the surface charge distribution, we were able to provide insight into the experimentally observed crystal phases. Our results indicate that for Qβ, the HCP crystal is observed at low polymer concentrations because it has a lower activation energy and not necessarily because it is the state with the lowest free energy. This is also supported by the observation that at higher polymer concentrations, where the experiments observe a transition from HCP to FCC, there is no longer a free-energy barrier for either crystal structure, in which case the virus particles will form an FCC structure, which we assume to be lower in absolute free energy. For MS-2 we see no difference in the barrier height and FCC should therefore be the only crystal phase observed, which is indeed what the experiments see.

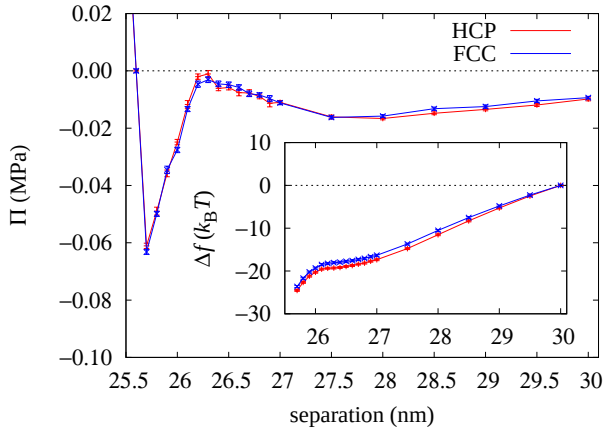

Figure 5.6: Osmotic pressure, Π, for the Qβ virus as a function of nearest-neighbor virus spacing for the HCP and FCC crystal structures with 50 mg/ml of 10 kDa PEG added. The pressure of both HCP and FCC is below zero beyond the stable separation. Δf as a function of nearest-neighbor virus spacing for the HCP and FCC crystal structures is shown in the inset. There is no free energy barrier for either structure.

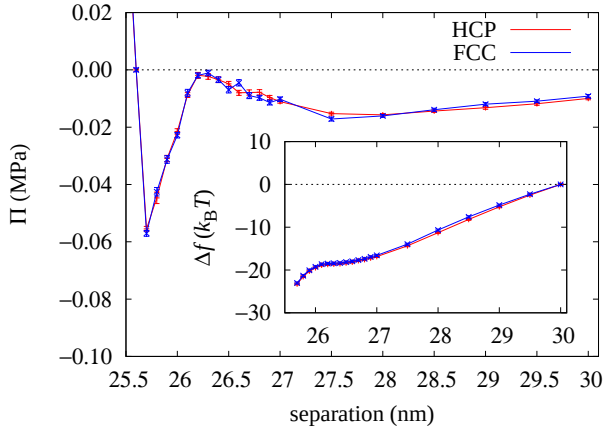

Figure 5.7: Osmotic pressure, Π, for the MS-2 virus as a function of nearest-neighbor virus spacing for the HCP and FCC crystal structures with 50 mg/ml of 10 kDa PEG added. The pressure of both HCP and FCC is below zero beyond the stable separation. Δf as a function of nearest-neighbor virus spacing for the HCP and FCC crystal structures is shown in the inset. There is no free energy barrier for either structure.

CHAPTER 6

FREEZE CASTING

The contents of this chapter are based on the following publication:

- **Stephen A. Barr** and Erik Luijten, Structural properties of materials created through freeze casting *Acta Materialia*, 58:709–715, 2010

In this chapter we examine the structure and dynamics of colloidal particles undergoing freeze casting. In this process, an aqueous suspension of solid particles is cast into a mold and subsequently frozen. The growing ice crystals generate ice fronts that concentrate the suspended particles in the intervening space. Upon removal of the ice through freeze drying, a porous, solid structure remains that can be sintered [11]. Although historically freeze casting has mostly been known for its flexibility and low cost, yielding materials with irregular structure [89], the use of directional freezing [90] permits remarkable control over the resulting pore structure. Indeed, this approach has been used to create a variety of structures, such as silica fiber bundles [90], tubular supports with radially aligned pores [91], and micro-honeycombs [92]. Freeze casting primarily employs suspensions of ceramic particles, but recently it also has been used to fabricate titanium foams with aligned, elongated pores [93]. The field received renewed attention with the work of Deville *et al.* [12,13], who demonstrated that complex composites can be built with lamellar microstructures that depend on the velocity of the freezing ice front and the initial conditions of the aqueous suspension. The porous scaffold obtained through freeze casting is backfilled with a second phase, resulting in a nacre-like material [12, 94].

Whereas various aspects of the freeze casting process, such as control over spacing between ice platelets [12, 13] and the interactions between an advancing ice front and colloidal particles [95, 96], have been explored previously, little is known about the arrangement of colloidal particles within the resulting structures. It is

therefore the purpose of this chapter to investigate by means of molecular dynamics simulations how details of the freezing process affect the resulting solid structure. In particular, we examine the role of ice front velocity and particle concentration. The simulations are restricted to an idealized model system, but we believe that nevertheless these simulations provide guidance for the creation of specific target structures.

6.1 Simulation details

We perform molecular dynamics simulations using a custom-modified version of the LAMMPS package [63]. To reproduce both the lamellar structure resulting from platelet-like ice crystals [12] and the honeycomb structures observed in Refs. [90, 92], we employ three-dimensional simulations in a planar and a columnar geometry. In the lamellar system, depicted schematically in Fig. 6.1, two parallel ice fronts (lateral area $10\,\mu\text{m} \times 10\,\mu\text{m}$) are placed initially 10 μm apart. As the platelets become thicker, these ice fronts advance towards each other (along the z-axis) at a constant velocity until they meet. In this case, we employ periodic boundary conditions in the x and y directions. The columnar geometry is generated by modeling the dendrites as rods that are arranged in a 2×2 hexagonal cell (Fig. 6.2). The rods are aligned along the z direction, with a nearest-neighbor spacing of 5 μm. During the simulation, their radius increases at a constant rate from 0 μm to 2.5 μm. The cell has a height of 10 μm and to minimize finite-size effects we replicate it periodically in all three dimensions, creating an infinite array of infinitely long dendrites.

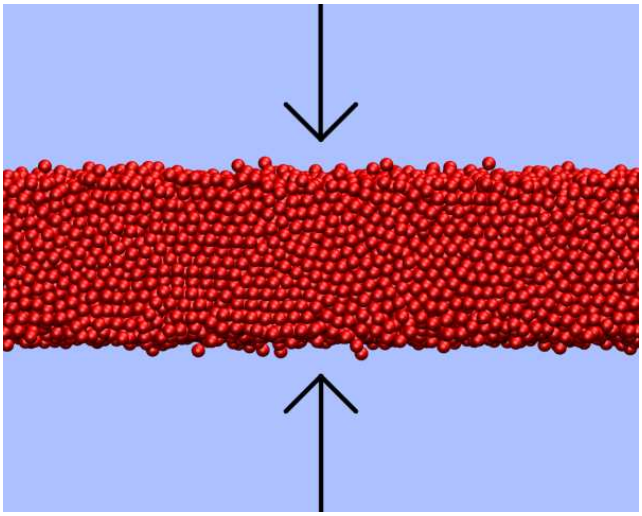

Figure 6.1: Schematic diagram of the lamellar geometry. The two planar ice fronts advance at a constant rate in the direction of the arrows, which run parallel to the z-axis. The fronts represent growing platelets that concentrate the suspended colloidal particles in the center region. All simulations are performed in three dimensions.

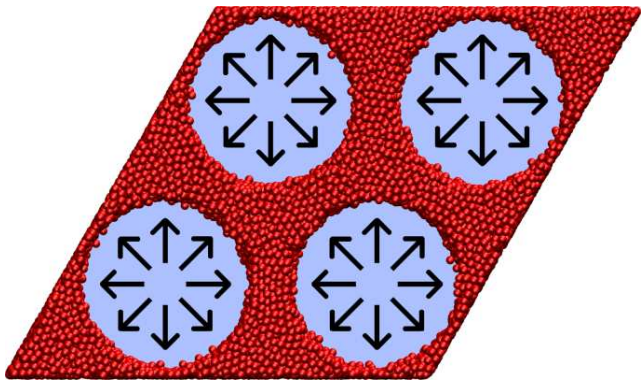

Figure 6.2: Schematic representation of the columnar geometry, looking down the z-axis. Cylindrical dendrites of ice form parallel to the z-axis and grow radially outward at a constant rate. As in Fig. 6.1, the solid particles are pushed into the intervening regions.

In both geometries, the suspended particles are modeled as monodisperse spheres that interact through a purely repulsive potential,

$$V(r) = k_{\mathrm{B}}T\left(\frac{\sigma}{r}\right)^{48}, \tag{6.1}$$

where $\sigma = 200$ nm is the diameter of the particles, k_{B} is Boltzmann's constant, and the temperature is set to $T = 273.15$ K, the freezing point for water. The potential is cut off at $r = 1.2\sigma$. All simulations are carried out in the NVT ensemble and the temperature is controlled by means of a Langevin thermostat. Initially, the particles are distributed homogeneously throughout the simulation cell and brought to thermal equilibrium. The interaction between the particles and the ice front is represented by the van der Waals potential for a sphere and a plane near contact [97]

$$W(h) = -\frac{AR}{6h}, \tag{6.2}$$

where $R = \sigma/2$ is the particle radius, A the Hamaker constant, and h the surface-to-surface distance between the ice front and the particle. For alumina particles (used in Ref. [12]) pushed by ice, $A = -2 \times 10^{-21}$ J, as calculated using Lifshitz theory [15]. Its negative value indicates a repulsive interaction [98, 99]. Our choice $\sigma = 200$ nm is comparable to the diameter of particles used in various experiments [12, 13, 89]. To make contact with recent experiments that employed titanium particles [93], we also investigate systems with $\sigma = 20$ μm. In this case $A = -7 \times 10^{-20}$ J [100]. For these large particles we only consider a columnar geometry, in which the dendrites have a nearest-neighbor spacing of 800 μm and the height of the simulation cell equals 1600 μm.

The repulsive interaction between the advancing ice front and the suspended particles causes the latter to be pushed into the interlamellar or interdendritic space, provided the front velocity, v_f, is less than the critical velocity, v_c. Once the front velocity exceeds this critical value, $v_\mathrm{f} > v_\mathrm{c}$, particles are engulfed by the ice front [13, 93, 99]. Particle engulfment has a twofold effect on the porous structures that are created during freeze casting: (i) It reduces the particle concentration in the space between the approaching ice fronts, allowing the growth of larger ice crystals, and hence larger pores, and (ii) the particles that are incorporated *within* the ice crystals can form narrow "linkers" of touching particles that, upon freeze drying, act as interconnects within the porous material. Such linkers have been observed in the lamellar structures formed by platelet-shaped ice crystals [12]. We incorporate this phenomenon in the molecular dynamics simulations by setting a distance δ, such that a particle is engulfed if its surface-to-surface distance to the ice front, h, is less than δ. Once engulfed, the particle remains stationary for the duration of the simulation. The distance δ is chosen such that the repulsive force exerted on the particle by the ice front equals the viscous drag force on the particle at the critical velocity, v_c. For alumina particles of diameter 200 nm pushed by ice in water, $v_\mathrm{c} = 125$ μm/s [93, 99]. The drag force F_d is calculated from Stokes' law,

$$F_\mathrm{d} = 6\pi\eta R v_\mathrm{c} \,, \tag{6.3}$$

where $\eta = 1.8$ cP is the viscosity of water at $T = 273.15$ K. By setting the frictional force used in the Langevin thermostat to correspond to the solvent viscosity, we arrive at a simulation method that takes into account particle engulfment. This method ignores the effect of gravity, the curvature of the ice front, and the influence the particles have on the shape of the ice front. While other simulation studies have used more detailed models of the interactions between a particle and an advancing solidification front [95,96,101–103], these have focused on a single colloidal particle. In contrast, our simplified model allows us to consider realistic particle concentrations and front velocities while capturing the important aspects of the engulfment process, including the collective behavior of large numbers of particles. Our simulations involve 35 000 to 280 000 particles and took up to 1600 CPU hours per run. In total, 51 runs were performed to cover all parameter choices, requiring 4 months of CPU time on a quad-core Intel Xeon E5472 processor.

6.2 Results

6.2.1 Evolution of colloidal volume fraction upon ice crystal growth

We first present the results for particles with a diameter of 200 nm. To determine the effect of front velocity, we investigate six different values of v_f, namely 2, 20, 40, 60, 80, and 100 μm/s. These values span the range of experimentally achievable front velocities [12]. We also investigate the role of colloid concentration by considering three different values of the initial volume fraction, $\phi_\mathrm{i} = 0.15$, 0.25, and 0.35. It is worth noting that the front velocity plays a role in determining whether the ice crystals form as platelets or dendrites [13]. However, in our calculations we have treated front velocity and geometry as independent parameters.

As the platelets or dendrites grow, the volume accessible to the particles decreases. At the same time some of the particles become engulfed, reducing the number of free particles in the system. Particles can be engulfed even if $v_\mathrm{f} < v_\mathrm{c}$ if particles have a sufficiently high velocity towards the ice front or if they are surrounded by other particles which force them into the ice front [104]. Because of this, the volume fraction of particles in the aqueous phase, ϕ, changes as the ice crystals grow. As an example, this is illustrated for a lamellar geometry in Fig. 6.3, which shows ϕ as a function of the distance d each of the ice fronts has traveled. We also indicate the corresponding width of the gap between the ice fronts, $\Delta = 10\ \mu\mathrm{m} - 2d$. Most of the particles are pushed, with only a small fraction being engulfed, and ϕ increases monotonically. This behavior continues until a volume fraction $\phi \approx 0.65$ is reached, i.e., close to the random close-packed volume fraction. For $\phi_\mathrm{i} = 0.15$ and $v_\mathrm{f} = 2\ \mu$m/s this occurs at $d = 19.5\sigma$, or a gap width $\Delta = 2.2\ \mu$m. At this point, the colloidal particles form a solid which prevents the particles closest to the ice front from being pushed farther. For higher front velocities, this point occurs at larger values of d (thicker platelets) since more particles are engulfed before a solid is formed and a smaller gap volume is required to reach the same volume fraction. After this, the ice front moves through the solid, pushing the remaining particles only over short distances, typically a fraction of their diameter σ, before engulfing them. Interestingly, the lowest front velocity, $v_\mathrm{f} = 2\mu$m/s, does not result in the largest final volume fraction. This can be understood as follows. As the system approaches solid-like densities, the pressure becomes large enough to force the particles into the ice front. At the lowest front velocity, more time is spent in this state and consequently more particles are engulfed. This, however is not a large effect and the difference in volume fraction between $v_\mathrm{f} = 2\ \mu$m/s and $v_\mathrm{f} = 20\ \mu$m/s is less than 0.03.

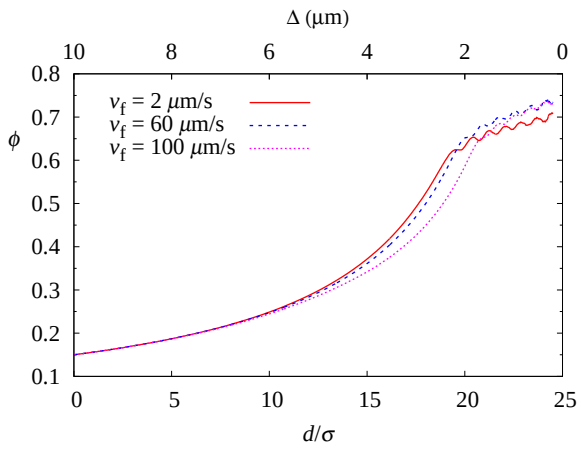

Figure 6.3: Volume fraction of colloids in the liquid phase, ϕ, as a function of the distance d each of the approaching ice fronts has traveled, for the lamellar geometry and an initial volume fraction $\phi_i = 0.15$. The top axis shows the width Δ of the gap between the platelets. The volume fraction increases gradually and monotonically until a value of $\phi \approx 0.65$ is reached, at which point the colloids form a solid. As the ice moves through this solid, the volume fraction increases more slowly and the oscillations observed are due to the ice moving through layers of particles, (*cf.* Fig. 6.6).

The behavior for the columnar geometry (Fig. 6.4) is quite similar, although there is no dependence on front velocity until the random close-packed volume fraction is reached, indicating that there is a lesser tendency of particle engulfment in this geometry.

6.2.2 Structure of solid phase

Our simulations do not only provide information on the evolution of the system as the ice crystals grow, but also permit investigation of the resulting solid colloidal phase. Once the colloids have been compressed into a dense state, the ice front continues to invade this phase, engulfing the colloids. Colloidal rearrangements may still occur at this stage, depending on front velocity. For the lamellar geometry, the freezing process is complete when neighboring ice fronts meet, i.e., at $d = 5\ \mu$m (25σ). For the columnar geometry, this point (*viz.* $d = 12.5\sigma = 2.5\ \mu$m) marks the end of isotropic radial growth of the dendrites; the ice will continue to invade the interstitial voids, but we do not observe any further displacement of the colloids. In the experimental system, the ice is subsequently removed through sublimation and loose particles (i.e., those that are disconnected from the solid structure) have to be disregarded. In our simulations, we determine which particles remain by means of a cluster-finding algorithm that identifies groups of connected particles. For this purpose we define two particles as connected if their surfaces are separated by less than 10 nm. Figure 6.5 shows the final configurations of the particles which would remain after the ice is removed for

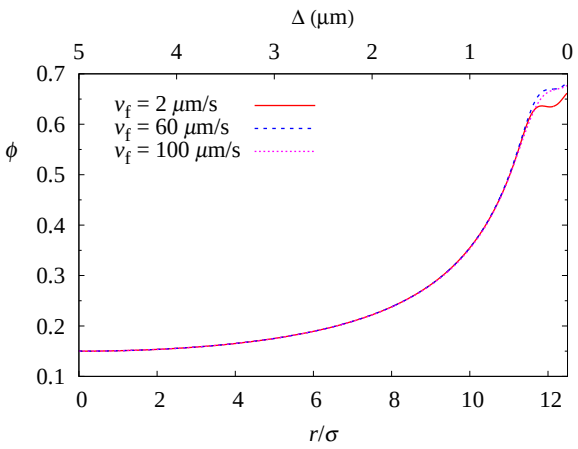

Figure 6.4: Volume fraction ϕ of colloids in the liquid phase as a function of the dendrite radius r, for the columnar geometry and an initial volume fraction $\phi_i = 0.15$. The graph also shows the width Δ of the interdendritic space, as measured along the center-to-center axis between neighboring dendrites. The volume fraction increases gradually and monotonically until a value of $\phi \approx 0.65$ is reached, at which point the colloids form a solid. As the ice moves through the solid, ϕ increases more slowly.

$\phi_i = 0.35$ and a range of front velocities. As mentioned, higher front velocities lead to thinner colloidal configurations since more particles are engulfed before a solid is formed. In Ref. [12], some of the engulfed particles were found to form bridges that link neighboring colloidal domains, thus mimicking the inorganic bridges that are found in nacre (*cf.* also Ref. [94]). Although we did not observe such bridges in our simulations, we found that higher front velocities result in rougher surfaces, since the particles have less time to rearrange as they are being pushed. This effect is more pronounced for higher initial volume fractions. The ability to manipulate the surface roughness is desirable, as it can be exploited to influence the bonding between the colloidal phase and the second phase that is backfilled into the pores left by the sublimated ice.

Our results for the columnar geometry corroborate the role played by particle engulfment in determining the thickness and surface structure of the colloidal phase. Indeed, since virtually no engulfment is observed in this case (*cf.* Fig. 6.4), we observe hardly any difference in wall thickness and surface roughness for different front velocities.

Inspection of the configurations depicted in Fig. 6.5 suggests that, for low front velocities, the particles form layers that are aligned parallel to the ice front. This observation is confirmed in Fig. 6.6, which shows the density profile in the direction perpendicular to the ice front, $\rho(z)$, for an initial volume fraction $\phi_i = 0.25$ and three different front velocities. The density profile not only emphasizes the dependence on front velocity, but also shows more pronounced layering near the edges (surfaces) of the dense phase. This arises because the colloids in the outer layers have been pushed over larger distances prior to being engulfed,

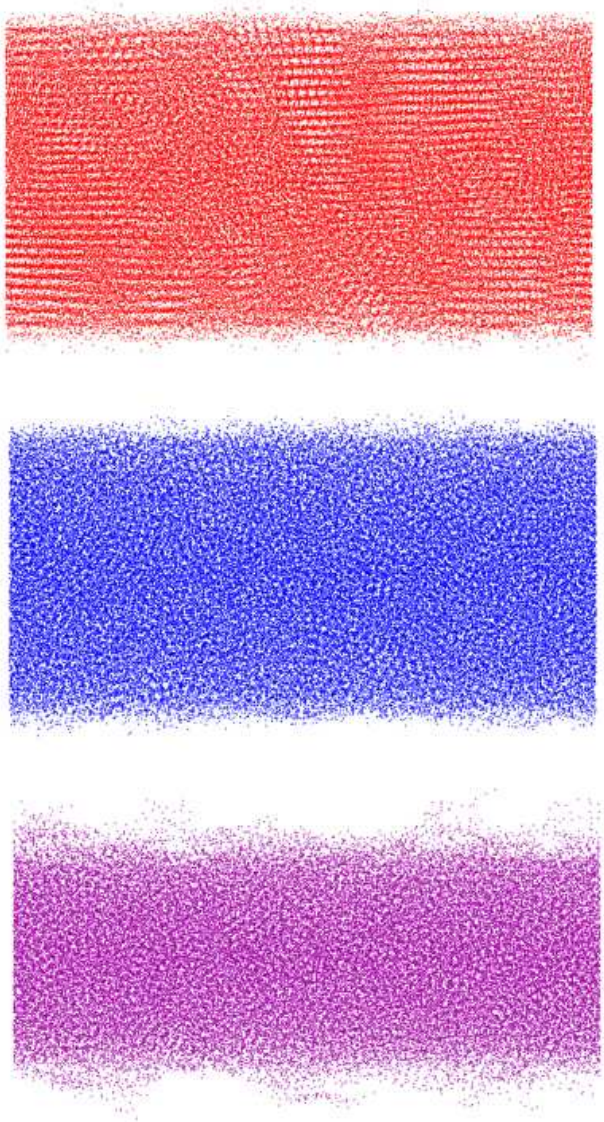

Figure 6.5: Final configuration of particles which remain after sublimation for $v_f = 2$ μm/s (top), $v_f = 40$ μm/s (middle), and $v_f = 100$ μm/s (bottom) for an initial volume fraction $\phi_i = 0.35$ in the lamellar geometry. The particles are depicted as points for clarity. Lower front velocities lead to thicker walls since fewer particles are engulfed, and higher front velocities result in rougher surfaces. For $v_f = 2$ μm/s, layers are clearly visible.

allowing the system to arrange into a more regular structure. The question then arises if regular colloidal arrangements can be observed *within* a layer, at least for the outer layers at the lowest front velocities. To determine this, we probe the two-dimensional pair correlation function $g_{2d}(r)$ within a slab that contains the layer closest to the surface. As can be seen in Fig. 6.7, there is no long-range order, even when well-defined layers are formed, and the peaks are indicative of a liquid-like arrangement. The front velocity has little effect on the structure within a layer; even though the nearest-neighbor peak is highest for $v_f = 2$ μm/s, the behavior at larger distances is independent of v_f. We find qualitatively similar results for other layers, and for different initial volume fractions.

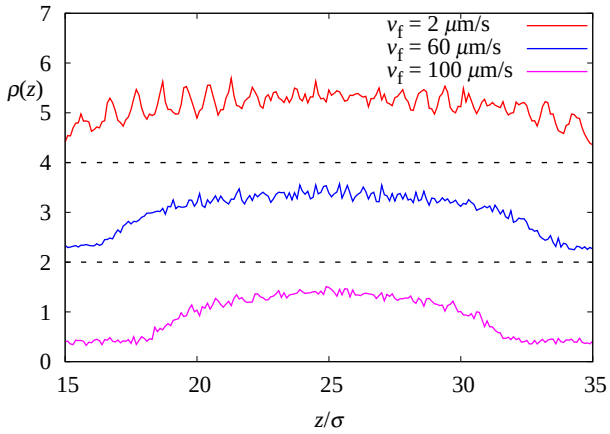

Figure 6.6: Density profile $\rho(z)$ of the final configuration of the particles for the lamellar geometry and $\phi_i = 0.25$. Different front velocities are offset for clarity with $v_f = 2$ μm/s (top), $v_f = 60$ μm/s (middle), and $v_f = 100$ μm/s (bottom). For $v_f = 2$ μm/s there are well-defined layers that are not seen for the higher front velocities. Note that for these higher velocities $\rho(z)$ does not decay to zero outside the center region because of particle engulfment.

In analogy with these observations, we find for the columnar geometry that low front velocities result in the formation of cylindrical shells around the dendrites. This is quantified by means of the radial distribution function of the particles around the dendrites, $g_{\mathrm{d,p}}(r)$, as shown in Fig. 6.8 for $\phi_{\mathrm{i}} = 0.15$. Interestingly, although Fig. 6.4 shows that virtual no particle engulfment takes place in this geometry and hence the evolution of the colloidal volume fraction is practically independent of front velocity, we find that the *structure* within the compressed phase varies strongly with front velocity. For $v_{\mathrm{f}} = 100$ μm/s, a layered structure no longer develops. The intra-layer structure is characterized by means of the two-dimensional pair correlation function calculated within a cylindrical shell containing the first particle layer (corresponding to the leftmost peak in Fig. 6.8). Like for the lamellar geometry, we observe clear peaks, but there is no long-range order (see inset of Fig. 6.7).

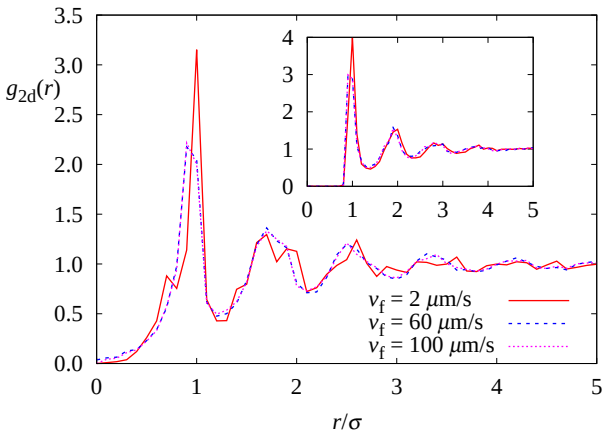

Figure 6.7: Two-dimensional pair correlation function $g_{2\mathrm{d}}(r)$ for the lamellar geometry, calculated within a planar slab (parallel to the advancing ice front) that contains the particle layer closest to the surface. The initial volume fraction is $\phi_{\mathrm{i}} = 0.25$ and curves for three different front velocities are shown. Even for $v_{\mathrm{f}} = 2$ μm/s, when well-defined layers form (*cf.* Fig. 6.6), no long-range order is observed within a layer. Higher front velocities show similar behavior. The inset shows the same quantity for the columnar geometry. In this case, $g_{2\mathrm{d}}(r)$ is calculated within a region bounded by two concentric cylindrical shells around a dendrite, chosen such that the region contains the particle layer closest to the ice front (i.e., the surface layer of the resulting solid structure).

6.2.3 Role of particle size

For both lamellar and columnar geometries, we conclude that layers form for lower front velocities because the particles have enough time to rearrange as they aggregate in front of the advancing ice. This can be confirmed by comparing the diffusive behavior of the particles to the front velocity. Using the drag force computed in Eq. (6.3), we obtain a diffusion coefficient $D = 1.11 \times 10^{-12}$ m^2/s. Accordingly, a particle will

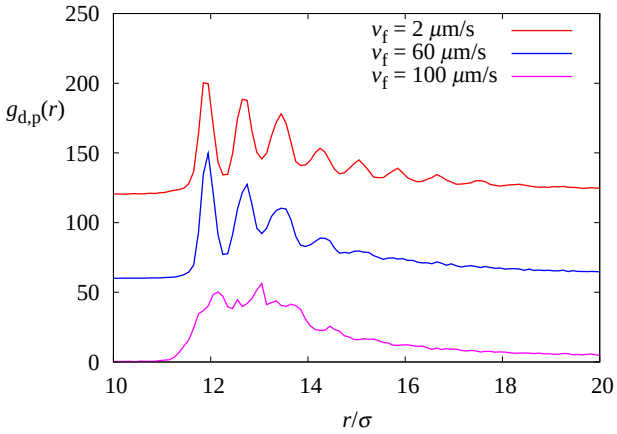

Figure 6.8: Radial distribution function $g_{d,p}(r)$ of the particles around the dendrites, for the columnar geometry with an initial volume fraction $\phi_i = 0.15$. Different front velocities are offset for clarity, with $v_f = 2$ μm/s (top), $v_f = 60$ μm/s (middle), and $v_f = 100$ μm/s (bottom). The peaks in $g_{d,p}(r)$ correspond to layers of particles forming concentric cylindrical shells around the dendrites. Lower front velocities result in well-defined layers not observed for the highest front velocity, $v_f = 100$ μm/s.

diffuse over a distance equal to its own diameter in 6×10^{-3} s, whereas it takes a front velocity of 33 μm/s to push the particle over the same distance in the same time. This is indeed consistent with the observation that we see well-ordered layers for $v_f = 2$ μm/s but not for $v_f = 100$ μm/s. Although we do not observe a sharp transition from order to disorder, the diffusion coefficient can be used to estimate how slowly the ice front must advance to obtain a layered structure. For example, for much larger particles with $\sigma = 20$ μm (comparable to the coarse titanium powder employed in Ref. [93]), the diffusion coefficient is 100 times smaller at $D = 1.11 \times 10^{-14}$ m^2/s. In this case it takes 6000 s for a particle to diffuse over its diameter and an ice front advancing at 3.3×10^{-3} μm/s would push the particle over the same distance in that time. Because of this slow diffusion rate, particles are unable to rearrange as they are pushed at typical front velocities, and long-range order cannot be achieved. To demonstrate this, we simulate these larger particles in a columnar geometry with a nearest-neighbor spacing between dendrites of 800 μm and measure the radial distribution function $g_{d,p}(r)$ in the final configuration, as shown in Fig. 6.9 for $v_f = 1$ μm/s and $\phi_i = 0.15$. There are no well-defined layers and the structure resembles what is observed for $\sigma = 200$ nm at $v_f = 100$ μm/s (Fig. 6.8).

The second effect that arises when larger particles are employed is the decrease in critical front velocity, v_c. For 200 nm particles, the front velocities we employ are always less than v_c and thus in all cases only a small fraction of the particles are engulfed before a solid is formed (*cf.* Figs. 6.3 and 6.4). However, for $\sigma = 20$ μm different behavior is observed. The critical front velocity for this system is 37 μm/s [93] and

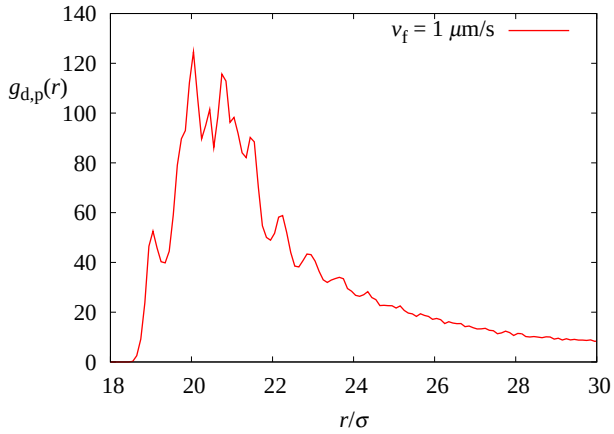

Figure 6.9: Radial distribution function $g_{d,p}(r)$ of large particles (diameter $\sigma = 20$ μm, initial volume fraction $\phi_i = 0.15$) around dendrites in a columnar geometry with a nearest-neighbor separation of 800 μm. In this counterpart of Fig. 6.8 (which pertains to particles with a 100 times smaller diameter), no layers are formed around the dendrites, even at the lowest front velocity of 1 μm/s.

thus the range of front velocities that result in pushing of particles is diminished. Also, within that range, we find that the front velocity has a larger effect on the final volume fraction of the system. This is illustrated in Fig. 6.10, which is the counterpart of Fig. 6.4, showing the instantaneous volume fraction of particles for different values of v_f at a fixed initial volume fraction of $\phi_i = 0.15$. If the front velocity exceeds 30 μm/s, particles are never pushed and thus remain homogeneously distributed. Front velocities of 10 μm/s and 20 μm/s do result in particles being pushed over long distances and the volume fraction in the interdendritic regions increases; however, many particles are still engulfed and the final volume fractions are not high enough for a solid to form. Only at the lowest front velocity of 1 μm/s a sufficient number of particles are pushed to form a solid. From this, we see that for large particle sizes the front velocity only affects the fraction of particles that are engulfed, not the structure of the resulting solid phase.

6.3 Summary and conclusions

Cryo-chemical methods hold significant promise for the manufacturing of nano- and microscale materials. Motivated by the recent experimental demonstration that freeze casting can be employed to fabricate composite materials with a well-controlled microstructure, we have investigated the effects of ice front velocity, ice crystal shape (lamellar and dendritic), particle concentration, and particle size on the properties of systems undergoing freeze casting. Since our molecular dynamics simulations focus on large-scale structural properties and involve several 100 000 particles, we have employed a simplified model of the engulfment

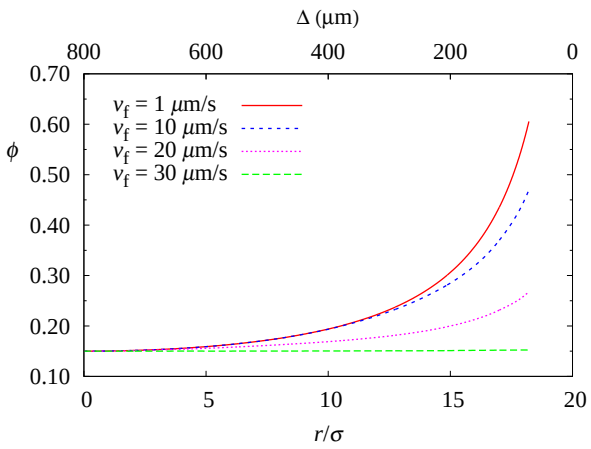

Figure 6.10: Volume fraction ϕ of unengulfed particles (diameter $\sigma = 20$ μm) as a function of the dendrite radius r, for the columnar geometry and an initial volume fraction $\phi_i = 0.15$. The top axis shows the width Δ of the interdendritic space. Compared to particles with a smaller diameter (Fig. 6.4), significant numbers of particles are engulfed, even at front velocities well below the critical front velocity.

process.

For submicron particles, we find that lower front velocities enable particles to rearrange while they are pushed by the ice front, resulting in a solid phase that is ordered in the direction of the crystal growth. In addition, the front velocity affects the fraction of particles that are engulfed by the advancing ice front, which in turn controls the thickness of the solid phases that are formed between the ice crystals. For large particles (diameter 20 μm), the front velocity has a much greater effect on the number of particles that are engulfed, even well below the critical front velocity, and low ice front velocities are required to create a solid phase. Furthermore, the diffusivity of these large particles is too small to permit the formation of ordered structures as the ice front advances.

To our knowledge this is the first attempt to employ molecular dynamics simulations for the investigation of a system undergoing freeze casting. Although our approach involves a number of simplifications, such as the assumption of monodisperse particles, the neglect of gravitational effects, and the stochastic modeling of the engulfment process, we believe that it may foster insight into the effect of various process variables on the resulting "green body" and serve as a starting point for further simulations. For example, our method could be extended to determine if the freezing of suspensions containing a mixture of colloidal particles of different sizes (such as a binary mixture) can be used to enhance materials properties. Furthermore, the structures obtained in our simulations could be used as input for sintering calculations.

CHAPTER 7

OUTLOOK

This work has focused on the study of colloidal particles using computer simulations. There are a variety of factors which can influence colloidal interactions and the structures they form. Here we have investigated two such factors, the presence of smaller particles in the colloidal suspension and the effect of an advancing ice front.

In Chapters 2, 3, and 4, we employed the GCA to determine the effective interactions between colloidal particles induced by a smaller species, either highly charged nanoparticles, charged rods, or multivalent counterions. In addition to the effective interactions, it would be interesting to investigate liquid-vapor phase separation in these systems. Owing to the size asymmetry, standard simulation methods are very inefficient. Recently, however, the GCA has been implemented in the restricted Gibbs ensemble to study the effect of small particles on the liquid-vapor coexistence of a Lennard-Jones fluid [105]. This method could in principle be applied to study phase separation of colloids in a system containing highly charged nanoparticles or charged rods. Implementing this to study phase separation of like-charged colloids with multivalent counterions poses a much more difficult problem, though. When particles are exchanged between boxes using cluster moves in the restricted Gibbs ensemble, the charge in each box will in general, not remain neutral. Because of this, the Ewald sum fails to yield the correct energy of each box, which is essential to the Monte Carlo method. This problem is not easily remedied. Only accepting cluster moves which maintain charge neutrality is inefficient because this will only occur in a very small fraction of cluster moves. On the other hand, exchanging additional particles after the cluster move has been completed to maintain charge neutrality leads to very low acceptance rates, as many particles have to be exchanged using the standard acceptance criterion for particle exchanges in the Gibbs ensemble [106].

In Chapter 5 we investigated the effect of two different species, non-adsorbing polymer and divalent salt, on the resulting structure of virus particles. While our simulations helped to understand the experimental results, there is still much to study in this system. One outstanding question is how the charge distribution

influences the orientations of the virus particles in the crystal and how this, in turn, influences the formation of different crystal structures. In this case, the icosahedral symmetry of the virus particles does not match either the FCC or the HCP crystals. Understanding the underlying effects of this mismatch on crystal formation is not only important for this particular system, but can be applied to systems of other patchy particles as well.

We also investigated the structure of colloidal particles pushed by an advancing ice front in the freeze casting process. Using a simplified model of the ice-particle interaction we were able to study the collective motion and structure of large numbers of colloidal particles. Another simplification we made is only including excluded volume interaction between the particles. Controlling the interparticle interaction could provide an additional way to control the structure of the resulting solid. Freeze casting a suspension of colloids with different surface charge distributions, for example, could lead to different structures, similar to what we found in Chapter 5. A possible way to enhance the mechanical properties of materials made by freeze casting is to use mixtures of different sized particles, so that the smaller particles fill in the space between the larger particles. These smaller particles, however, will also alter the effective interactions between the large particles. As we found in Chapter 2, different concentrations of small particles can result in either stabilization or flocculation of the larger particles and this, by itself, will influence the resulting structure. Understanding both of these effects would allow for optimization of the mechanical properties.

By studying mixtures of large and small particles, we can determine the important factors which influence the range, strength, and shape of the resulting effective interactions between the large particles. Understanding this can provide insight into new ways to control colloidal interactions. In addition, these effective interactions are also important in determining the resulting structures colloidal particles form, either in equilibrium or in non-equilibrium systems such as particles being pushed by an ice front. While this thesis has explored many different systems independently, the results obtained are an important step towards having greater control over colloidal structure and interactions.

REFERENCES

[1] J. E. Smay, J. Cesarano, III and J. A. Lewis, "Colloidal inks for directed assembly of 3-D periodic structures," Langmuir **18**, 5429–5437 (2002).

[2] M. L. Taylor, G. E. Morris and R. S. C. Smart, "Influence of aluminum doping on titania pigment structural and dispersion properties," J. Colloid Interface Sci. **262**, 81–88 (2003).

[3] M. J. Kogan, N. G. Bastus, R. Amigo, D. Grillo-Bosch, E. Araya, A. Turiel, A. Labarta, E. Giralt and V. F. Puntes, "Nanoparticle-mediated local and remote manipulation of protein aggregation," Nano Letters **6**, 110–115 (2006).

[4] P. V. Braun and P. Wiltzius, "Electrochemically grown photonic crystals," Nature **402**, 603–604 (1999).

[5] D. M. Herlach, I. Klassen, P. Wette and D. Holland-Moritz, "Colloids as model systems for metals and alloys: a case study of crystallization," J. Phys.: Condens. Matter **22**, 153101 (2010).

[6] A. T. Chan and J. A. Lewis, "Electrostatically tuned interactions in silica microsphere-polystyrene nanoparticle mixtures," Langmuir **21**, 8576–8579 (2005).

[7] V. Tohver, J. E. Smay, A. Braem, P. V. Braun and J. A. Lewis, "Nanoparticle halos: A new colloid stabilization mechanism," Proc. Natl. Acad. Sci. U.S.A. **98**, 8950–8954 (2001).

[8] S. Asakura and F. Oosawa, "Interaction between particles suspended in solutions of macromolecules," J. Polym. Sci. **33**, 183–192 (1958).

[9] J. Liu and E. Luijten, "Rejection-free geometric cluster algorithm for complex fluids," Phys. Rev. Lett. **92**, 035504 (2004).

[10] J. Liu and E. Luijten, "Generalized geometric cluster algorithm for fluid simulation," Phys. Rev. E **71**, 066701 (2005).

[11] T. Fukasawa, M. Ando, T. Ohji and S. Kanzaki, "Synthesis of porous ceramics with complex pore structure by freeze-dry processing," J. Am. Ceram. Soc. **84**, 230–232 (2001).

[12] S. Deville, E. Saiz, R. K. Nalla and A. P. Tomsia, "Freezing as a path to build complex composites," Science **311**, 515–518 (2006).

[13] S. Deville, E. Saiz and A. P. Tomsia, "Ice-templated porous alumina structures," Acta. Mater. **55**, 1965–1974 (2007).

[14] E. J. Verwey and J. T. G. Overbeek, *Theory of the Stability of Lyophobic Colloids* (Elsevier, Amsterdam, 1948).

[15] J. N. Israelachvili, *Intermolecular and Surface Forces*, 2nd ed. (Academic, San Diego, 1992).

[16] V. Tohver, A. Chan, O. Sakurada and J. A. Lewis, "Nanoparticle engineering of complex fluid behavior," Langmuir **17**, 8414–8421 (2001).

[17] J. Liu and E. Luijten, "Stabilization of colloidal suspensions by means of highly charged nanoparticles," Phys. Rev. Lett. **93**, 247802 (2004).

[18] J. Liu and E. Luijten, "Colloidal stabilization via nanoparticle halo formation," Phys. Rev. E **72**, 061401 (2005).

[19] S. Karanikas and A. A. Louis, "Dynamic colloidal stabilization by nanoparticle halos," Phys. Rev. Lett. **93**, 248303 (2004).

[20] R. J. Hunter, *Foundations of Colloid Science*, 2nd ed. (Oxford University Press, Oxford, 2001).
[21] D. C. Prieve and W. B. Russel, "Simplified predictions of Hamaker constants from Lifshitz theory," J. Colloid Interface Sci. **125**, 1–13 (1988).
[22] M. Dijkstra, R. van Roij and R. Evans, "Phase diagram of highly asymmetric binary hard-sphere mixtures," Phys. Rev. E **59**, 5744–5771 (1999).
[23] A. A. Louis and R. Roth, "Generalized depletion potentials," J. Phys.: Condens. Matter **13**, L777–L784 (2001).
[24] R. Roth, R. Evans and A. A. Louis, "Theory of asymmetric nonadditive binary hard-sphere mixtures," Phys. Rev. E **64**, 051202 (2001).
[25] R. Roth, R. Evans and S. Dietrich, "Depletion potential in hard-sphere mixtures: Theory and applications," Phys. Rev. E **62**, 5360–5377 (2000).
[26] S. Asakura and F. Oosawa, "On interaction between two bodies immersed in a solution of macromolecules," J. Chem. Phys. **22**, 1255–1256 (1954).
[27] B. Götzelmann, R. Roth, S. Dietrich, M. Dijkstra and R. Evans, "Depletion potential in hard-sphere fluids," Europhys. Lett. **47**, 398–404 (1999).
[28] D. Rudhardt, C. Bechinger and P. Leiderer, "Direct measurement of depletion potentials in mixtures of colloids and nonionic polymers," Phys. Rev. Lett. **81**, 1330-1333 (1998).
[29] R. Verma, J. C. Crocker, T. C. Lubensky and A. G. Yodh, "Entropic colloidal interactions in concentrated dna solutions," Phys. Rev. Lett. **81**, 4004 (1998).
[30] R. Roth, "Depletion potentials in colloidal mixtures of spheres and rods," J. Phys.: Condens. Matter **15**, S277–S282 (2003).
[31] L. Helden, G. H. Koenderink, P. Leiderer and C. Bechinger, "Depletion potentials induced by charged rods," Langmuir **20**, 5662–5665 (2004).
[32] Y. Mao, M. E. Cates and H. N. W. Lekkerkerker, "Depletion force in colloidal systems," Physica A **222**, 10–24 (1995).
[33] Y. Mao, M. E. Cates and H. N. W. Lekkerkerker, "Theory of the depletion force due to rodlike polymers," J. Chem. Phys. **106**, 3721–3729 (1997).
[34] M. Schmidt, "Density functional theory for colloidal rod-sphere mixtures," Phys. Rev. E **63**, 050201 (2001).
[35] R. Roth, "Depletion potentials in colloidal mixtures of spheres and rods," J. Phys.: Condens. Matter **15**, S277–S282 (2003).
[36] W. Li, T. Yang and H. Ma, "Depletion potentials in colloidal mixtures of hard spheres and rods," J. Chem. Phys. **128**, 044910 (2008).
[37] P. Bolhuis and D. Frenkel, "Numerical study of the phase diagram of a mixture of spherical and rodlike molecules," J. Chem. Phys. **101**, 9869–9875 (1994).
[38] W. B. Russel, D. A. Saville and W. R. Schowalter, *Colloidal Dispersions* (Cambridge University Press, Cambridge, U.K., 1989).
[39] H. H. von Grünberg, L. Helden, P. Leiderer and C. Bechinger, "Measurement of surface charge densities on brownian particles using total internal reection microscopy," J. Chem. Phys. **114**, 10094–10104 (2001).
[40] N. Metropolis, A. W. Rosenbluth, M. N. Rosenbluth, A. H. Teller and E. Teller, "Equation of state calculations by fast computing machines," J. Chem. Phys. **21**, 1087–1092 (1953).
[41] D. Frenkel and B. Smit, *Understanding Molecular Simulation*, 2nd ed. (Academic, San Diego, 2002).
[42] M. P. Allen and D. J. Tildesley, *Computer Simulation of Liquids* (Clarendon, Oxford, 1987).
[43] P. Bolhuis and D. Frenkel, "Tracing the phase boundaries of hard spherocylinders," J. Chem. Phys. **106**, 666–687 (1997).
[44] A. A. Louis, E. Allahyarov, H. Löwen and R. Roth, "Effective forces in colloidal mixtures: From depletion attraction to accumulation repulsion," Phys. Rev. E **65**, 061407 (2002).

[45] B. V. Derjaguin and L. Landau, "," Acta Physicochim. USSR **14**, 633–662 (1941).
[46] N. Grønbech-Jensen, K. M. Beardmore and P. Pincus, "Interactions between charged spheres in divalent counterion solution," Physica A **261**, 74–81 (1998).
[47] J. Wu, D. Bratko and J. M. Prausnitz, "Interaction between like-charged colloidal spheres in electrolyte solutions," Proc. Natl. Acad. Sci. U.S.A. **95**, 15169–15172 (1998).
[48] P. Linse and V. Lobaskin, "Electrostatic attraction and phase separation in solutions of like-charged colloidal particles," Phys. Rev. Lett. **83**, 4208–4211 (1999).
[49] P. Linse and V. Lobaskin, "Electrostatic attraction and phase separation in solutions of like-charged colloidal particles," J. Chem. Phys. **112**, 3917–3927 (2000).
[50] B. Hribar and V. Vlachy, "Clustering of macroions in solutions of highly asymmetric electrolytes," Biophys. J. **78**, 694–698 (2000).
[51] E. Allahyarov, I. D'Amico and H. Löwen, "Attraction between like-charged macroions by Coulomb depletion," Phys. Rev. Lett. **81**, 1334–1337 (1998).
[52] I. Rouzina and V. A. Bloomfield, "Macroion attraction due to electrostatic correlation between screening counterions. 1. Mobile surface-adsorbed ions and diffuse ion cloud," J. Phys. Chem. **100**, 9977–9989 (1996).
[53] A. Naji and R. R. Netz, "Attraction of like-charged macroions in the strong-coupling limit," Eur. Phys. J. E **13**, 43–59 (2004).
[54] A. Naji, S. Jungblut, A. G. Moreira and R. R. Netz, "Electrostatic interactions in strongly coupled soft matter," Physica A **352**, 131–170 (2005).
[55] P. P. Ewald, "Die Berechnung optischer und elektrostatischer Gitterpotentiale," Ann. Phys. (Leipzig) **369**, 253–287 (1921).
[56] S. W. de Leeuw, J. W. Perram and E. R. Smith, "Simulation of electrostatic systems in periodic boundary conditions. I. Lattice sums and dielectric constants," Proc. R. Soc. London, Ser. A **373**, 27–56 (1980).
[57] C. Dress and W. Krauth, "Cluster algorithm for hard spheres and related systems," J. Phys. A **28**, L597–L601 (1995).
[58] J. G. Malherbe and S. Amokrane, "Asymmetric mixture of hard particles with Yukawa attraction between unlike ones: a cluster algorithm simulation study," Mol. Phys. **97**, 677–683 (1999).
[59] J. W. Perram, H. G. Petersen and S. W. de Leeuw, "An algorithm for the simulation of condensed matter which grows as the $\frac{3}{2}$ power of the number of particles," Mol. Phys. **65**, 875–893 (1988).
[60] J. Kolafa and J. W. Perram, "Cutoff errors in the Ewald summation formula for point charge systems," Mol. Simul. **9**, 351–368 (1992).
[61] D. Fincham, "Optimisation of the Ewald sum for large systems," Mol. Simul. **13**, 1–9 (1994).
[62] K. Binder and E. Luijten, "Monte Carlo tests of renormalization-group predictions for critical phenomena in Ising models," Phys. Rep. **344**, 179–253 (2001).
[63] S. J. Plimpton, "Fast parallel algorithms for short-range molecular dynamics," J. Comp. Phys. **117**, 1–19 (1995).
[64] R. W. Hockney and J. W. Eastwood, *Computer Simulation Using Particles* (IOP Publishing, Bristol, 1988).
[65] S. Alexander, P. M. Chaikin, P. Grant, G. J. Morales and P. Pincus, "Charge renormalization, osmotic pressure, and bulk modulus of colloidal crystals: Theory," J. Chem. Phys. **80**, 5776–5781 (1984).
[66] L. Bocquet, E. Trizac and M. Aubouy, "Effective charge saturation in colloidal suspensions," J. Chem. Phys. **117**, 8138–8152 (2002).
[67] S. Pianegonda, E. Trizac and Y. Levin, "The renormalized jellium model for spherical and cylindrical colloids," J. Chem. Phys. **126**, 014702 (2007).
[68] V. Lobaskin and P. Linse, "Accurate simulation of highly asymmetric electrolytes with charge asymmetry 20:1 and 20:2," J. Chem. Phys. **109**, 3530–3541 (1998).

[69] V. Lobaskin and P. Linse, "Simulation of an asymmetric electrolyte with charge asymmetry 60:1 using hard-sphere and soft-sphere models," J. Chem. Phys. **111**, 4300–4309 (1999).

[70] S. C. Glotzer and M. J. Solomon, "Anisotropy of building blocks and their assembly into complex structures," Nature Mater. **6**, 557–562 (2007).

[71] N. Schmidt, S. Barr, A. Udit, L. Gutierrez, T. Nguyen, M. G. Finn, E. Luijten and G. Wong, "Structural transitions in condensed colloidal virus phases," Bull. Am. Phys. Soc. **54**, (2010).

[72] L. V. Woodcock, "Entropy difference between the face-centred cubic and hexagonal close-packed crystal structures," Nature **385**, 141–143 (1997).

[73] P. G. Bolhuis, D. Frenkel, S. Mau and D. A. Huse, "Entropy difference between crystal phases," Nature **388**, 235–236 (1997).

[74] A. D. Bruce, N. B. Wilding and G. J. Ackland, "Free energy of crystalline solids: A lattice-switch Monte Carlo method," Phys. Rev. Lett. **79**, 3002–3005 (1997).

[75] M. Carrillo-Tripp, C. M. Shepherd, I. A. Borelli, S. Venkataraman, G. Lander, P. Natarajan, J. E. Johnson, C. L. B. III and V. S. Reddy, "VIPERdb^2: an enhanced and web API enabled relational database for structural virology," Nucl. Acids Res. **37**, D436–D442 (2008).

[76] R. Golmohammadi, K. Fridborg, M. Bundule, K. Valegrd and L. Liljas, "The crystal structure of bacteriophage Qβ at 3.5 å resolution," Structure **4**, 543–554 (1996).

[77] D. A. Kuzmanovic, I. Elashvili, C. Wick, C. O'Connell and S. Krueger, "Bacteriophage MS2: Molecular weight and spatial distribution of the protein and RNA components by small-angle neutron scattering and virus counting," Structure **11**, 1339–1348 (2003).

[78] T. J. Dolinsky, J. E. Nielsen, J. A. McCammon and N. A. Baker, "PDB2PQR: an automated pipeline for the setup of poissonboltzmann electrostatics calculations," Nucl. Acids Res. **32**, W665–W667 (2004).

[79] T. J. Dolinsky, P. Czodrowski, H. Li, J. E. Nielsen, J. H. Jensen, G. Klebe and N. A. Baker, "PDB2PQR: expanding and upgrading automated preparation of biomolecular structures for molecular simulations," Nucl. Acids Res. **35**, W522–W525 (2007).

[80] H. Li, A. D. Robertson and J. H. Jensen, "Very fast empirical prediction and rationalization of protein pK_a values," Proteins: Struct., Fucnt., Bioinf. **61**, 704–721 (2005).

[81] R. H. Hardin, N. J. A. Sloane and W. D. Smith, "Tables of spherical codes with icosahedral symmetry", published electronically at http://www.research.att.com/ njas/icosahedral.codes/, 2000.

[82] L. R. Overby, G. H. Barlow, R. H. Doi, M. Jacob and S. Spiegelman, "Comparison of two serologically distinct ribonucleic acid bacteriophages," J. Bacteriol. **91**, 442–448 (1966).

[83] J. A. Redman, S. B. Grant and T. M. Olson, "Filtration of recombined norwalk virus particles and bacteriophage MS2 in quartz sand: Importance of electrostatic interactions," Environ. Sci. Technol. **31**, 3378–3383 (1997).

[84] J. P. Valleau and L. K. Cohen, "Primitive model electrolytes. I. Grand canonical Monte Carlo computations," J. Chem. Phys. **72**, 5935–5941 (1980).

[85] D. N. Theodorou, T. D. Boone, L. R. Dodd and K. F. Mansfield, "Stress tensor in model polymer systems with periodic boundaries," Makromol. Chem. Theory Simul. **2**, 191–238 (1993).

[86] T. L. Hill, *Statistical Mechanics: Principles and Selected Applications* (McGraw-Hill, New York, 1956).

[87] A. P. Lyubartsev, J. X. Tang, P. A. Janmey and L. Nordenskiöld, "Electrostatically induced polyelectrolyte association of rodlike virus particles," Phys. Rev. Lett. **81**, 5465–5468 (1998).

[88] C. Guáqueta, L. K. Sanders, G. C. L. Wong and E. Luijten, "The effect of salt on self-assembled actin–lysozyme complexes," Biophys. J. **90**, 4630–4638 (2006).

[89] S. W. Sofie and F. Dogan, "Freeze casting of aqueous alumina slurries with glycerol," J. Am. Ceram. Soc. **84**, 1459–1464 (2001).

[90] W. Mahler and M. F. Bechtold, "Freeze-formed silica fibres," Nature **285**, 27–28 (1980).
[91] J.-W. Moon, H.-J. Hwang, M. Awano and K. Maeda, "Preparation of NiO–YSZ tubular support with radially aligned pore channels," Mat. Lett. **57**, 1428–1434 (2003).
[92] S. R. Mukai, H. Nishihara and H. Tamon, "Formation of monolithic silica gel microhoneycombs (SMHs) using pseudosteady state growth of microstructural ice crystals," Chem. Commun. 874–875 (2004).
[93] Y. Chino and D. C. Dunand, "Directionally freeze-cast titanium foam with aligned, elongated pores," Acta. Mater. **56**, 105–113 (2008).
[94] E. Munch, M. E. Launey, D. H. Alsem, E. Saiz, A. P. Tomsia and R. O. Ritchie, "Tough, bio-inspired hybrid materials," Science **322**, 1516–1520 (2008).
[95] J. W. Garvin and H. S. Udaykumar, "Particle–solidification front dynamics using a fully coupled approach, part II: comparison of drag expressions," J. Cryst. Growth **252**, 467–479 (2003).
[96] J. W. Garvin, Y. Yang and H. S. Udaykumar, "Multiscale modeling of particle–solidification front dynamics. Part II: Pushing-engulfment transition," Int. J. Heat Mass Tran. **50**, 2969–2980 (2007).
[97] V. A. Parsegian, *Van der Waals Forces* (Cambridge University Press, Cambridge, 2006).
[98] J. Visser, "The concept of negative Hamaker coefficients. 1. History and present status," Adv. Colloid Interface Sci. **15**, 157–169 (1981).
[99] P. Casses and M. A. Azouni-Aidi, "A general theoretical approach to the behaviour of foreign particles at advancing solid–liquid interfaces," Adv. Colloid Interface Sci. **50**, 103–120 (1994).
[100] I. Larson, C. J. Drummond, D. Y. C. Chan and F. Grieser, "Direct force measurements between TiO_2 surfaces," J. Am. Chem. Soc. **115**, 11885–11890 (1993).
[101] J. W. Garvin and H. S. Udaykumar, "Particle–solidification front dynamics using a fully coupled approach, Part I: methodology," J. Cryst. Growth **252**, 451–466 (2003).
[102] J. W. Garvin and H. S. Udaykumar, "Effect of a premelted film on the dynamics of particle–solidification front interactions," J. Cryst. Growth **290**, 602–614 (2006).
[103] J. W. Garvin, Y. Yang and H. S. Udaykumar, "Multiscale modeling of particle–solidification front dynamics, Part I: Methodology," Int. J. Heat Mass Tran. **50**, 2952–2968 (2007).
[104] Y. M. Youssef, R. J. Dashwood and P. D. Lee, "Effect of clustering on particle pushing and solidification behaviour in TiB_2 reinforced aluminium PMMCs," Composites Part A **36**, 747–763 (2005).
[105] J. Liu, N. B. Wilding and E. Luijten, "Simulation of phase transitions in highly asymmetric fluid mixtures," Phys. Rev. Lett. **97**, 115705 (2006).
[106] A. Z. Panagiotopoulos, "Direct determination of phase coexistence properties of fluids by Monte Carlo simulation in a new ensemble," Mol. Phys. **61**, 813–826 (1987).

AUTHOR'S BIOGRAPHY

Stephen Barr was born in 1981 in Springboro, Ohio. He studied at the Ohio State University from 2000 to 2004 where he obtained a B.S. in Physics. In 2004, he joined the Material Science and Engineering Department at the University of Illinois at Urbana-Champaign, where he joined Prof. Erik Luijten's research group. His research focused on using computer simulations to study the effective interactions of colloidal particles.